

Strange Baryon Production in Hadronic Z^0 Decays

OPAL Collaboration

Abstract

The production of the $J^P = \frac{1}{2}^+$ octet baryons Λ and Ξ^- , the $J^P = \frac{3}{2}^+$ decuplet baryons $\Sigma(1385)^\pm$, $\Xi(1530)^0$, and Ω^- , and the $J^P = \frac{3}{2}^-$ orbitally excited state $\Lambda(1520)$ has been measured in a sample of approximately 3.65 million hadronic Z^0 decays. The integrated rates and the differential cross-sections as a function of x_E , the scaled energy, are determined. The differential cross-sections of the Λ and Ξ^- baryons are found to be softer than those predicted by both the JETSET and HERWIG Monte Carlo generators. The measured baryon yields are found to disagree with the simple diquark picture where only one tuning parameter for spin 1 diquarks is allowed. The yields are further compared with a thermodynamic model of hadron production which includes the production of orbitally excited mesons and baryons. The momentum spectra of Λ , Ξ^- , $\Sigma(1385)^\pm$, $\Xi(1530)^0$, and $\Lambda(1520)$ are also compared to the predictions of an analytical QCD formula.

(Submitted to Zeitschrift für Physik C)

The OPAL Collaboration

G. Alexander²³, J. Allison¹⁶, N. Altekamp⁵, K. Ametewee²⁵, K.J. Anderson⁹, S. Anderson¹²,
S. Arcelli², S. Asai²⁴, D. Axen²⁹, G. Azuelos^{18,a}, A.H. Ball¹⁷, E. Barberio⁸, R.J. Barlow¹⁶,
R. Bartoldus³, J.R. Batley⁵, J. Bechtluft¹⁴, C. Beeston¹⁶, T. Behnke⁸, A.N. Bell¹, K.W. Bell²⁰,
G. Bella²³, S. Bentvelsen⁸, P. Berlich¹⁰, S. Bethke¹⁴, O. Biebel¹⁴, V. Blobel⁸, I.J. Bloodworth¹,
J.E. Bloomer¹, M. Bobinski¹⁰, P. Bock¹¹, H.M. Bosch¹¹, M. Boutemour³⁴, B.T. Bouwens¹²,
S. Braibant¹², R.M. Brown²⁰, H.J. Burckhart⁸, C. Burgard⁸, R. Bürgin¹⁰, P. Capiluppi²,
R.K. Carnegie⁶, A.A. Carter¹³, J.R. Carter⁵, C.Y. Chang¹⁷, C. Charlesworth⁶, D.G. Charlton^{1,b},
D. Chrisman⁴, S.L. Chu⁴, P.E.L. Clarke¹⁵, I. Cohen²³, J.E. Conboy¹⁵, O.C. Cooke¹⁶,
M. Cuffiani², S. Dado²², C. Dallapiccola¹⁷, G.M. Dallavalle², S. De Jong¹², L.A. del Pozo⁸,
K. Desch³, M.S. Dixit⁷, E. do Couto e Silva¹², M. Doucet¹⁸, E. Duchovni²⁶, G. Duckeck³⁴,
I.P. Duerdoth¹⁶, J.E.G. Edwards¹⁶, P.G. Estabrooks⁶, H.G. Evans⁹, M. Evans¹³, F. Fabbri²,
P. Fath¹¹, F. Fiedler¹², M. Fierro², H.M. Fischer³, R. Folman²⁶, D.G. Fong¹⁷, M. Foucher¹⁷,
A. Fürtjes⁸, P. Gagnon⁷, A. Gaidot²¹, J.W. Gary⁴, J. Gascon¹⁸, S.M. Gascon-Shotkin¹⁷,
N.I. Geddes²⁰, C. Geich-Gimbel³, F.X. Gentit²¹, T. Geralis²⁰, G. Giacomelli², P. Giacomelli⁴,
R. Giacomelli², V. Gibson⁵, W.R. Gibson¹³, D.M. Gingrich^{30,a}, D. Glenzinski⁹, J. Goldberg²²,
M.J. Goodrick⁵, W. Gorn⁴, C. Grandi², E. Gross²⁶, M. Gruwé⁸, C. Hajdu³², G.G. Hanson¹²,
M. Hansroul⁸, M. Hapke¹³, C.K. Hargrove⁷, P.A. Hart⁹, C. Hartmann³, M. Hauschild⁸,
C.M. Hawkes⁵, R. Hawkings⁸, R.J. Hemingway⁶, G. Herten¹⁰, R.D. Heuer⁸, M.D. Hildreth⁸,
J.C. Hill⁵, S.J. Hillier¹, T. Hilse¹⁰, P.R. Hobson²⁵, R.J. Homer¹, A.K. Honma^{28,a}, D. Horváth^{32,c},
R. Howard²⁹, R.E. Hughes-Jones¹⁶, D.E. Hutchcroft⁵, P. Igo-Kemenes¹¹, D.C. Imrie²⁵,
M.R. Ingram¹⁶, K. Ishii²⁴, A. Jawahery¹⁷, P.W. Jeffreys²⁰, H. Jeremie¹⁸, M. Jimack¹, A. Joly¹⁸,
C.R. Jones⁵, G. Jones¹⁶, M. Jones⁶, R.W.L. Jones⁸, U. Jost¹¹, P. Jovanovic¹, T.R. Junk⁸,
D. Karlen⁶, K. Kawagoe²⁴, T. Kawamoto²⁴, R.K. Keeler²⁸, R.G. Kellogg¹⁷, B.W. Kennedy²⁰,
B.J. King⁸, J. Kirk²⁹, S. Kluth⁸, T. Kobayashi²⁴, M. Kobel¹⁰, D.S. Koetke⁶, T.P. Kokott³,
S. Komamiya²⁴, R. Kowalewski⁸, T. Kress¹¹, P. Krieger⁶, J. von Krogh¹¹, P. Kyberd¹³,
G.D. Lafferty¹⁶, H. Lafoux²¹, R. Lahmann¹⁷, W.P. Lai¹⁹, D. Lanske¹⁴, J. Lauber¹⁵,
S.R. Lautenschlager³¹, J.G. Layter⁴, D. Lazic²², A.M. Lee³¹, E. Lefebvre¹⁸, D. Lellouch²⁶,
J. Letts², L. Levinson²⁶, C. Lewis¹⁵, S.L. Lloyd¹³, F.K. Loebinger¹⁶, G.D. Long¹⁷, M.J. Losty⁷,
J. Ludwig¹⁰, A. Luig¹⁰, A. Malik²¹, M. Mannelli⁸, S. Marcellini², C. Markus³, A.J. Martin¹³,
J.P. Martin¹⁸, G. Martinez¹⁷, T. Mashimo²⁴, W. Matthews²⁵, P. Mättig³, W.J. McDonald³⁰,
J. McKenna²⁹, E.A. Mckigney¹⁵, T.J. McMahon¹, A.I. McNab¹³, R.A. McPherson⁸, F. Meijers⁸,
S. Menke³, F.S. Merritt⁹, H. Mes⁷, J. Meyer²⁷, A. Michelini², G. Mikenberg²⁶, D.J. Miller¹⁵,
R. Mir²⁶, W. Mohr¹⁰, A. Montanari², T. Mori²⁴, M. Morii²⁴, U. Müller³, K. Nagai²⁶,
I. Nakamura²⁴, H.A. Neal⁸, B. Nellen³, B. Nijhar¹⁶, R. Nisius⁸, S.W. O'Neale¹, F.G. Oakham⁷,
F. Odorici², H.O. Ogren¹², T. Omori²⁴, M.J. Oreglia⁹, S. Orito²⁴, J. Pálinkás^{33,d}, G. Pásztor³²,
J.R. Pater¹⁶, G.N. Patrick²⁰, J. Patt¹⁰, M.J. Pearce¹, S. Petzold²⁷, P. Pfeifenschneider¹⁴,
J.E. Pilcher⁹, J. Pinfold³⁰, D.E. Plane⁸, P. Poffenberger²⁸, B. Poli², A. Posthaus³,
H. Przysieznik³⁰, D.L. Rees¹, D. Rigby¹, S.A. Robins¹³, N. Rodning³⁰, J.M. Roney²⁸,
A. Rooke¹⁵, E. Ros⁸, A.M. Rossi², M. Rosvick²⁸, P. Routenburg³⁰, Y. Rozen²², K. Runge¹⁰,
O. Runolfsson⁸, U. Ruppel¹⁴, D.R. Rust¹², R. Rylko²⁵, K. Sachs¹⁰, E.K.G. Sarkisyan²³,
M. Sasaki²⁴, C. Sbarra², A.D. Schaile³⁴, O. Schaile³⁴, F. Scharf³, P. Scharff-Hansen⁸, P. Schenk⁴,
B. Schmitt⁸, S. Schmitt¹¹, M. Schröder⁸, H.C. Schultz-Coulon¹⁰, M. Schulz⁸, M. Schumacher³,
P. Schütz³, W.G. Scott²⁰, T.G. Shears¹⁶, B.C. Shen⁴, C.H. Shepherd-Themistocleous²⁷,
P. Sherwood¹⁵, G.P. Siroli², A. Sittler²⁷, A. Skillman¹⁵, A. Skuja¹⁷, A.M. Smith⁸, T.J. Smith²⁸,

G.A. Snow¹⁷, R. Sobie²⁸, S. Söldner-Rembold¹⁰, R.W. Springer³⁰, M. Sproston²⁰, A. Stahl³,
M. Starks¹², M. Steiert¹¹, K. Stephens¹⁶, J. Steuerer²⁷, B. Stockhausen³, D. Strom¹⁹,
F. Strumia⁸, P. Szymanski²⁰, R. Tafrout¹⁸, S.D. Talbot¹, S. Tanaka²⁴, P. Taras¹⁸, S. Tarem²²,
M. Tecchio⁸, M. Thiergen¹⁰, M.A. Thomson⁸, E. von Törne³, S. Towers⁶, T. Tsukamoto²⁴,
E. Tsur²³, A.S. Turcot⁹, M.F. Turner-Watson⁸, P. Utzat¹¹, R. Van Kooten¹², G. Vasseur²¹,
M. Verzocchi¹⁰, P. Vikas¹⁸, M. Vinciter²⁸, E.H. Vokurka¹⁶, F. Wäckerle¹⁰, A. Wagner²⁷,
C.P. Ward⁵, D.R. Ward⁵, J.J. Ward¹⁵, P.M. Watkins¹, A.T. Watson¹, N.K. Watson⁷, P. Weber⁶,
P.S. Wells⁸, N. Wermes³, J.S. White²⁸, B. Wilkens¹⁰, G.W. Wilson²⁷, J.A. Wilson¹, G. Wolf²⁶,
S. Wotton⁵, T.R. Wyatt¹⁶, S. Yamashita²⁴, G. Yekutieli²⁶, V. Zacek¹⁸,

¹School of Physics and Space Research, University of Birmingham, Birmingham B15 2TT, UK

²Dipartimento di Fisica dell' Università di Bologna and INFN, I-40126 Bologna, Italy

³Physikalisches Institut, Universität Bonn, D-53115 Bonn, Germany

⁴Department of Physics, University of California, Riverside CA 92521, USA

⁵Cavendish Laboratory, Cambridge CB3 0HE, UK

⁶Ottawa-Carleton Institute for Physics, Department of Physics, Carleton University, Ottawa, Ontario K1S 5B6, Canada

⁷Centre for Research in Particle Physics, Carleton University, Ottawa, Ontario K1S 5B6, Canada

⁸CERN, European Organisation for Particle Physics, CH-1211 Geneva 23, Switzerland

⁹Enrico Fermi Institute and Department of Physics, University of Chicago, Chicago IL 60637, USA

¹⁰Fakultät für Physik, Albert Ludwigs Universität, D-79104 Freiburg, Germany

¹¹Physikalisches Institut, Universität Heidelberg, D-69120 Heidelberg, Germany

¹²Indiana University, Department of Physics, Swain Hall West 117, Bloomington IN 47405, USA

¹³Queen Mary and Westfield College, University of London, London E1 4NS, UK

¹⁴Technische Hochschule Aachen, III Physikalisches Institut, Sommerfeldstrasse 26-28, D-52056 Aachen, Germany

¹⁵University College London, London WC1E 6BT, UK

¹⁶Department of Physics, Schuster Laboratory, The University, Manchester M13 9PL, UK

¹⁷Department of Physics, University of Maryland, College Park, MD 20742, USA

¹⁸Laboratoire de Physique Nucléaire, Université de Montréal, Montréal, Quebec H3C 3J7, Canada

¹⁹University of Oregon, Department of Physics, Eugene OR 97403, USA

²⁰Rutherford Appleton Laboratory, Chilton, Didcot, Oxfordshire OX11 0QX, UK

²¹CEA, DAPNIA/SPP, CE-Saclay, F-91191 Gif-sur-Yvette, France

²²Department of Physics, Technion-Israel Institute of Technology, Haifa 32000, Israel

²³Department of Physics and Astronomy, Tel Aviv University, Tel Aviv 69978, Israel

²⁴International Centre for Elementary Particle Physics and Department of Physics, University of Tokyo, Tokyo 113, and Kobe University, Kobe 657, Japan

²⁵Brunel University, Uxbridge, Middlesex UB8 3PH, UK

²⁶Particle Physics Department, Weizmann Institute of Science, Rehovot 76100, Israel

²⁷Universität Hamburg/DESY, II Institut für Experimental Physik, Notkestrasse 85, D-22607 Hamburg, Germany

²⁸University of Victoria, Department of Physics, P O Box 3055, Victoria BC V8W 3P6, Canada

²⁹University of British Columbia, Department of Physics, Vancouver BC V6T 1Z1, Canada

³⁰University of Alberta, Department of Physics, Edmonton AB T6G 2J1, Canada

³¹Duke University, Dept of Physics, Durham, NC 27708-0305, USA

³²Research Institute for Particle and Nuclear Physics, H-1525 Budapest, P O Box 49, Hungary

³³Institute of Nuclear Research, H-4001 Debrecen, P O Box 51, Hungary

³⁴Ludwigs-Maximilians-Universität München, Sektion Physik, Am Coulombwall 1, D-85748 Garching, Germany

^a and at TRIUMF, Vancouver, Canada V6T 2A3

^b and Royal Society University Research Fellow

^c and Institute of Nuclear Research, Debrecen, Hungary

^d and Department of Experimental Physics, Lajos Kossuth University, Debrecen, Hungary

1 Introduction

Baryon¹ production in e^+e^- annihilation can be used to study the process of fragmentation of quarks and gluons into observable hadrons. At present no calculable theoretical description of this process exists. Since the inclusive differential momentum spectra of mesons and baryons are observed to be very similar, it is assumed that they are also produced by similar mechanisms during the fragmentation process. However, the measured production ratio of Ξ^- to Λ and the small production rates of decuplet baryons require additional mechanisms to suppress the production of baryons with strangeness and with spin $\frac{3}{2}$.

The observed momentum spectra and the extra suppression factors can be described by the diquark model [1], the most common approach used to describe baryon production in jets. According to this scheme, quark-antiquark and diquark-antidiquark pairs are produced from the sea. A diquark combines with a quark to form a baryon. This scheme, as used within the Lund string model [2] and implemented within the JETSET Monte Carlo [3] for example, implies similar fragmentation functions for baryons and light mesons. Several parameters in the model can be tuned to try to reproduce measured production rates, including a parameter to suppress the production of spin 1 diquarks relative to spin 0 diquarks. In the cluster fragmentation model, which is based on a different picture of hadron formation, hadrons are produced by the isotropic decays of colourless clusters formed from quark-antiquark pairs. Although there are fewer tunable parameters in such models, such as HERWIG [4], inclusive particle rates have some sensitivity to the maximum cluster mass.

Baryon and meson cross-sections have been measured at PETRA and PEP as well as at LEP [5]. From these results it can be concluded that although the fragmentation models implemented in the JETSET [3] and HERWIG [4] Monte Carlo describe the overall event shapes in e^+e^- annihilation well, they fail in some important details. In particular, at LEP energies the differential cross-sections of protons [6–8] and Λ baryons [9–12] have been measured to be softer than predicted by the models, while those of charged [6–8] and neutral [11–14] kaons are harder than predicted. In addition, measurements of the tensor mesons $f_2(1270)$, $K_2^*(1430)$, and $f_2'(1525)$ have shown that states with orbital angular momentum have significant production rates [14–17], which motivates the search for the production of orbitally excited baryons, which so far have not been included in JETSET or HERWIG.

The $\Lambda(1520)$ is the only orbitally excited baryon to have been measured in e^+e^- annihilation, at a centre-of-mass energy of 10 GeV [18]. It has a narrow width of 15.6 ± 1.0 MeV [19] and decays into charged hadrons (pK^- with a branching ratio of 22.5% [19]), which should be easily observable, allowing a good isolation of the signal. By comparing the $\Lambda(1520)$ production rate with those of the $\Sigma(1385)$ and the $\Xi(1530)^0$ one can see whether spin $\frac{3}{2}$ baryons with the same strangeness or with similar mass have comparable production rates.

In this note we report on the first measurement of $\Lambda(1520)$ production at LEP energies, and update our previous results on strange baryon cross-sections [9] for Λ , Ξ^- , $\Sigma(1385)^\pm$, $\Xi(1530)^0$, and Ω^- . In addition, new measurements of the Σ^+ , Σ^0 , and Σ^- baryons have recently been presented by OPAL in [20]. The present analysis is based on more than seven times the amount of data that was available in [9]. The analysis also benefits from a better understanding of the OPAL detector and its simulation. Therefore, systematic errors have been improved relative to our previous paper.

The paper is organised as follows. The OPAL detector and event samples are discussed in

¹To simplify the text, we use the term baryon to signify baryon plus antibaryon, unless explicitly stated otherwise.

Section 2. In Section 3 the selection criteria for the various strange baryons are given. The systematic errors which enter into the determinations of the cross sections are discussed in Section 4, and the cross-section measurements themselves are detailed in Section 5. Finally comparisons of the measurements with various QCD models and calculations are made in Section 6.

2 The OPAL Detector and Data Selection

OPAL is a multipurpose detector covering almost the entire solid angle around the interaction region at LEP. Details concerning the detector and its performance are given elsewhere [21]. This analysis relies mainly on the information from the central tracking chambers, which will be described here briefly.

Tracking of charged particles is performed by a central detector, consisting of a silicon microvertex detector [22], a vertex chamber, a jet chamber and z -chambers². The central detector is positioned inside a solenoid, which provides a uniform magnetic field of 0.435 T. The silicon microvertex detector consists of two layers of silicon strip detectors. The inner layer covers a polar angle range of $|\cos \theta| < 0.83$ and the outer layer covers $|\cos \theta| < 0.77$. The vertex chamber is a precision drift chamber which covers the range $|\cos \theta| < 0.95$. The jet chamber is a large volume drift chamber 4 m long and 3.7 m in diameter which provides tracking in the $r - \phi$ plane using up to 159 measured space points and in z by the charge division along the wires. The jet chamber also allows the measurement of the specific energy loss of charged particles, dE/dx . A resolution of 3.5% [23] has been obtained for tracks with $|\cos \theta| < 0.7$, allowing particle identification over a large momentum range. A precise measurement of the z -coordinate is provided by the z -chambers which surround the jet chamber and cover the range $|\cos \theta| < 0.72$. The combination of these chambers leads to a momentum resolution of $\sigma_{p_t}/p_t \approx \sqrt{0.02^2 + (0.0015 \cdot p_t)^2}$, p_t being the transverse track momentum with respect to the beam direction in GeV, and where the first term represents the contribution from multiple scattering.

This analysis is based on the data sample collected between 1990 and 1994 with centre-of-mass energies on or near the Z^0 peak. With the requirement that the central tracking chambers be operational a total of 3.65 million hadronic Z^0 decays has been selected using the criteria described in [24] with an efficiency of $(98.4 \pm 0.4)\%$. The remaining background processes, such as $e^+e^- \rightarrow \tau^+\tau^-$ and two photon events, were estimated to be at a negligible level (0.1% or less). For the measurement of the Λ cross-section, which is dominated by the systematic error, only the data up to and including 1993 are used.

To determine the selection efficiencies for the different baryons, we have used a sample of approximately 7.5 million JETSET 7.3 and JETSET 7.4 hadronic Z^0 decays which have been passed through the full OPAL detector simulation program [25]. The versions of JETSET have been tuned to agree with overall event shapes as measured by OPAL. Details of the parameters can be found in [26]. The two versions differ mostly in the tuning of the fragmentation parameters and the decay branching ratios of heavy flavour hadrons. For the measurement of the Λ cross-section only the JETSET 7.3 events are used, because these were processed with the simulation of the detector up to and including 1993. The JETSET 7.4 events were passed through a simulation of the detector corresponding to the 1994 data.

²In OPAL the coordinate system is defined such that the positive z -axis is along the direction of the electron beam, r is the coordinate normal to the beam axis, and θ and ϕ are the polar and azimuthal angles with respect to z , respectively.

3 Selection of Strange Baryons

The Λ , Ξ^- , and Ω^- baryons can be identified by their weak decays into $p\pi^-$ (63.9%), $\Lambda\pi^-$ (100%), and ΛK^- (67.8%), respectively [19]. Due to the long lifetimes of these weakly decaying baryons, combinatorial background can be strongly suppressed by selecting particle combinations with secondary vertices which are clearly displaced from the primary vertex³. The remaining background under the Ξ^- and Ω^- has been determined by using the wrong charge combinations, $\Lambda\pi^+$ and ΛK^+ , respectively.

The $\Sigma(1385)^\pm$, $\Xi(1530)^0$, and $\Lambda(1520)$ baryons decay strongly into $\Lambda\pi^\pm$ (88%), $\Xi^-\pi^+$ (67%), and pK^- (22.5%), respectively [19]. In these cases, no additional secondary vertex cuts are possible to reduce the combinatorial background. For these resonances, the background has been determined by fits to smooth background functions.

The selection criteria for the various strange baryons are detailed below. Discussion of the systematic errors on the measurements follow in Section 4.

3.1 The Λ Baryon

As in our previous publication [9], two methods were applied to select Λ baryons. The first method was optimised to have good mass and momentum resolution. The second method was optimised to give a higher efficiency over a broader Λ momentum range and was subsequently used to search for the other baryon species which decay to final states containing a Λ . The first method was used to determine the Λ cross-section because it has a smaller systematic error, although a consistent measurement of the cross-section over the entire x_E range was obtained using the second method.

3.1.1 Λ method 1

This method has been improved by including the endcap region of the OPAL detector ($0.7 < |\cos\theta| < 0.96$), leading to an increase in the geometrical acceptance of 30%. In the endcap region, a precise measurement of the θ -coordinate can be made using the radius of the last measured hit in the jet chamber [27]. In our previous analysis only tracks in the barrel region ($|\cos\theta| < 0.7$), which were required to have at least 4 associated z -chamber measurements, were considered.

All pairs of oppositely charged tracks which had more than 25% of the number of geometrically possible jet chamber hits and at least 20 hits, which had a transverse momentum relative to the beam direction (p_t) of more than 150 MeV, and which had a measurement of the θ -coordinate either in the z -chambers or in the endcap, were examined. The higher momentum track was taken to be the proton. Selected combinations were required to have at least one track pair intersection in the plane perpendicular to the beam axis which fulfilled the following criteria:

- the radial distance of the intersection point from the primary vertex was required to have been in the range 1 – 150 cm on the side of the primary vertex to which the combined momentum vector pointed;

³The primary vertex was fitted for each event using the measured track coordinates in the event. No attempt was made to explicitly exclude the tracks from decays of long-lived states, such as the Λ . However, since these tracks are generally well displaced from the interaction region, they are not often assigned to the primary vertex.

- if the distance from the primary vertex to the intersection point was less than 30 cm, the impact parameter transverse to the beam direction ($|d_0|$) of the pion with respect to the primary vertex must have been larger than 3 mm and the $|d_0|$ of the proton track larger than 1 mm;
- if the intersection point was reconstructed inside the jet chamber volume (the distance from the primary vertex to the intersection point was more than 30 cm) neither track must have had jet chamber hits more than 3 cm upstream towards the primary vertex;
- the angle in the plane transverse to the beam direction, Φ , between the direction of flight from the primary vertex to the intersection point and the reconstructed Λ momentum, was required to be smaller than 35 mrad.

If two valid intersections were found, the one closer to the beam axis was taken. To improve the resolution, low momentum tracks were corrected for energy loss within the detector material and the momenta of the two tracks were constrained in the z -direction to originate from a common secondary vertex. Background was further suppressed by using the measured dE/dx if more than 20 hits contributed to the dE/dx measurement of a track. Momentum dependent cuts were applied, as the separation in dE/dx between particle types varies with momentum:

- The higher momentum track was required to have
 - a $dE/dx > 8$ keV/cm and a probability⁴ of being consistent with a proton $W_p > 0.5\%$ if the track momentum satisfied $p < 1.5$ GeV;
 - a $dE/dx < 8.5$ keV/cm if the momentum was between $1.5 \text{ GeV} < p < 2 \text{ GeV}$, where protons and pions both have a specific energy loss of about 7 keV/cm;
 - $W_p > 5\%$ and $W_p > W_K$ if the momentum was $p > 2 \text{ GeV}$.
- For the lower momentum track the pion probability was required to be $W_\pi > 0.1\%$ over the entire momentum range.

Photon conversions were identified and removed if the invariant mass of the two tracks, assuming that they were an electron-positron pair, was smaller than 40 MeV.

With these cuts a narrow Λ mass peak was obtained above a small background as shown in figure 1. The mass was determined to be 1115.8 ± 0.1 MeV by fitting a Gaussian distribution to the peak and is in good agreement with the Particle Data Group value of 1115.7 MeV [19]. The resolution of the Λ mass is 2.4 ± 0.1 MeV.

The combinatorial background under the signal peak and the detection efficiency were determined for 15 different intervals of the scaled energy⁵, x_E , in the range $0.027 \leq x_E \leq 0.7$. Outside this range no significant Λ signal was observed. In each interval a background of the form $(1 - e^{-a(m-1.077)}) \times (bm + c)$ was fitted to the distribution of the invariant mass, m , measured in GeV. The fit was performed over a mass range between 1.08 GeV and 1.20 GeV, excluding the interval of ± 16 MeV around the nominal Λ mass which contains the Λ signal together with the non-Gaussian tails. The number of Λ baryons was counted within a signal region of ± 12 MeV around the Λ mass using the background estimated from the fit. A total of 94 877 Λ 's above a background of 39 126 was found (table 1).

⁴The difference between the measured and expected dE/dx for a given particle type, h , assuming a Gaussian distribution with a known width, defines the probability, W_h .

⁵Defined as $x_E \equiv 2 \cdot E_\Lambda / \sqrt{s}$, where \sqrt{s} is the centre-of-mass energy and E_Λ is the energy of the Λ candidate.

3.1.2 Λ method 2

The selection criteria for method 2 are unchanged from our previous publication [9]. The main difference from method 1 is that there is no requirement to have a precise θ -measurement for the tracks in either the z -chambers or in the endcap. This results in a higher efficiency over a broader momentum range although with an approximately 0.5 MeV worse mass resolution. The identified Λ candidates are then used to search for the other baryon species.

All pairs of oppositely charged tracks which passed the general track quality cuts of method 1 were examined and the higher momentum track was taken to be the proton. The $|d_0|$ of the proton candidate was required to be larger than 0.5 mm and the $|d_0|$ of the pion candidate larger than 3 mm. Background was suppressed by using the information from the dE/dx measurement, if available, as in method 1. Selected combinations were then required to have at least one track pair intersection within the radial range of 1 – 130 cm on the side of the primary vertex to which the combined momentum vector pointed. If two intersections were found, the one closer to the primary vertex was normally used. The second solution was used

- if both tracks had their first reconstructed hit after the second intersection point, or
- if one track had hits before and the other track had the first hit after the second intersection and the angle Φ (defined previously) was smaller than for the first intersection.

Candidates with hits on both tracks more than 5 cm upstream towards the primary vertex from the track intersection were removed. Then, in order to improve the mass resolution, the momentum components in the z -direction of the two tracks were constrained to originate from the average z -position of the tracks at the decay point if the measured radial decay distance was greater than 20 cm or if both tracks had hits in the z -chambers.

Additional cuts were then made in order to reduce background:

- the Φ angle of the Λ candidate was required to be smaller than 30 mrad and also smaller than $10 \text{ mrad} + 20 \text{ mrad}/p_t(\Lambda)$, where $p_t(\Lambda)$ is measured in GeV;
- if the reconstructed radius of the decay point was less than 25 cm, it was required that the primary vertex was found between the points of closest approach of the two tracks;
- a momentum dependent cut on the decay distance was applied. It was required that the probability of the Λ to have decayed after the calculated radial distance ($e^{-(m_\Lambda/p_t) \cdot (r/c\tau)}$, where $c\tau$ is the decay length, r the radial distance, and the other quantities are measured in GeV), be less than 95%. In addition, for small Λ transverse momentum ($p_t < 1 \text{ GeV}$), we required that this probability be greater than 2% (this latter cut excludes Λ baryons with very long decay distances);
- the angle θ^* between the proton direction in the Λ rest frame and the Λ direction was required to satisfy $|\cos \theta^*| < 0.98$;
- photon conversions were removed if the invariant mass of the track pair, assuming it to be an electron-positron pair, was smaller than 40 MeV.

Finally all Λ candidates with $|\cos \theta| < 0.9$ and $x_p > 0.01$ were retained, where $x_p \equiv p_\Lambda/2\sqrt{s}$ is the scaled momentum of the Λ and p_Λ is the momentum of the candidate. The resulting invariant mass distribution is shown in figure 2.

All Λ candidates whose mass fell within the signal region of ± 10 MeV around the Λ mass of 1116 MeV for $x_E < 0.2$ and within ± 15 MeV for larger x_E values were then used to identify the Ξ^- , $\Sigma(1385)^\pm$, $\Xi(1530)^0$, and Ω^- baryons, as described below. As a cross-check, we determined the Λ production cross-section and compared it to the results of method 1 (see Section 5). In order to do this, we estimated the background for method 2 by sideband subtraction, using the mass intervals between 1091 – 1101 MeV and 1131 – 1141 MeV. From a study of Monte Carlo⁶ events we found that this method underestimates the background in the signal region by 20% independent of the Λ momentum. The background estimated from the sidebands was therefore increased by this additional factor and subtracted from the events in the signal region. A total of 244 415 Λ 's above a background of 99 753 was reconstructed.

3.2 The Ξ^- Baryon

Ξ^- were identified by their weak decays to $\Lambda\pi^-$. Secondary vertices of Λ candidates and additional charged tracks, assumed to be pions, were selected using the following criteria:

- the $|d_0|$ of the additional pion track was required to be larger than 0.15 mm;
- if there were more than 20 hits available for the dE/dx measurement, the additional track was rejected if the dE/dx probability to be a pion was smaller than 5% and the probability to be an electron or a proton was larger than 5%;
- an intersection of the track and the Λ momentum vector must have been found in the $r - \phi$ plane within a radial range of 1 – 50 cm;
- the Φ angle (defined previously) of the $\Lambda\pi^-$ combination was required to be smaller than 30 mrad and also smaller than $10 \text{ mrad} + 20 \text{ mrad}/p_t(\Xi^-)$, where $p_t(\Xi^-)$ is measured in GeV;
- the scaled momentum of the Ξ^- candidate, x_p , was required to be greater than 0.02.

Figure 3 shows the narrow Ξ^- mass peak with some non-Gaussian tails obtained with these selection criteria. The number of Ξ^- candidates with a reconstructed invariant mass in the signal region between 1306 MeV and 1336 MeV is given in table 1.

The background under the Ξ^- signal was determined by using the wrong charge combination ($\Lambda\pi^+$). Since charge correlations exist between the pions, the background to the $\Lambda(\rightarrow p\pi^-)\pi^-$ invariant mass distribution is slightly lower than for $\Lambda(\rightarrow p\pi^-)\pi^+$. However, a study of Monte Carlo simulated events showed that apart from the overall normalisation, the wrong charge combination correctly estimated the shape of the background in the $\Lambda\pi^-$ invariant mass distribution. Therefore, a correction was made by scaling the wrong charge combination to obtain agreement for invariant masses more than 25 MeV away from the Ξ^- mass. This resulted in a 0.935 ± 0.011 normalisation scale factor in the data (applied in figure 3) and 0.891 ± 0.008 in the Monte Carlo. As a cross-check a fit to a third order polynomial background function and a Gaussian signal shape was made and was found to give consistent results for the number of signal events within 2% in both the data and Monte Carlo. The wrong charge combination was chosen as the background estimator because it resulted in a slightly smaller systematic error.

⁶For Λ method 2 and for the other baryons (Ξ^- , Ω^- etc.) the complete Monte Carlo sample consisting of both JETSET 7.3 and 7.4 events was used to determine selection efficiencies unless explicitly stated otherwise.

3.3 The Ω^- Baryon

Since the topology of $\Omega^- \rightarrow \Lambda K^-$ decays is the same as that of $\Xi^- \rightarrow \Lambda \pi^-$, the selection criteria are similar. The only differences from the Ξ^- selection are:

- the p_t of the additional track, which was assumed to be a kaon, was required to have been larger than 200 MeV;
- the kaon candidate was rejected if the dE/dx probability for a kaon was smaller than 5% or if fewer than 20 hits were available for the dE/dx measurement;
- the Φ angle (defined earlier) of the ΛK combination was required to be smaller than 20 mrad;
- combinations whose $\Lambda \pi^-$ mass fell within the Ξ^- signal region between 1306 and 1336 MeV were rejected.

With these selection criteria an Ω^- mass peak was observed as seen in figure 4.

As in the case of the Ξ^- , the estimate of the background using the wrong charge combination disagreed with the background outside the signal region. However, in the case of the Ω^- , the wrong charge combination underestimated rather than overestimated the background. The disagreement is also present in the Monte Carlo and it was found to be due to an excess of $\Lambda \bar{p}$ background combinations (total baryon number $|B| = 0$) compared to Λp ($|B| = 2$). This background was studied and it was found that by using the dE/dx requirements we could not eliminate this disagreement and still maintain a high efficiency. However, a study of both the data and the Monte Carlo samples (JETSET 7.3 and 7.4) showed that as in the case of the Ξ^- , the wrong charge combination ΛK^+ correctly described the shape of the background in the right charge combination ΛK^- , but was approximately $(16.9 \pm 1.8)\%$ too low in the Monte Carlo and $(10.7 \pm 2.2)\%$ too low in the data as determined from a fit for invariant masses more than 25 MeV away from the Ω^- mass. We therefore scaled the wrong charge combination, ΛK^+ , upwards by 1.107 ± 0.022 in the data in order to estimate the background under the Ω^- signal. In the data we found a total of 252 Ω^- candidates above a background of 960 in a signal region ± 20 MeV around the nominal Ω^- mass of 1672 MeV, as given in table 1.

3.4 The Decuplet Baryons $\Sigma(1385)^\pm$ and $\Xi(1530)^0$

The $\Sigma(1385)^\pm$ and $\Xi(1530)^0$ selections are based on those described in our previous analysis [9]. The methods to determine the background have been improved. The $\Sigma(1385)^+$, $\Sigma(1385)^-$, and $\Xi(1530)^0$ decay strongly to $\Lambda \pi^+$, $\Lambda \pi^-$, and $\Xi^- \pi^+$, respectively. The strong decays allow no further rejection of background by a secondary vertex finding technique. The dE/dx information was not used to reject non-pion tracks since the relatively small reduction in background did not offset the additional systematic uncertainties introduced by using dE/dx particle identification.

Good tracks which satisfied the same p_t and hit requirements as Λ method 1, and whose impact parameters with respect to the primary vertex were less than 2 mm, were assumed to be pions which originated from the interaction point. The invariant masses of all $\Lambda \pi^\pm$ and $\Xi^- \pi^+$ combinations were then calculated and are shown in figures 5, 6 and 7. In figure 5 one can see a $\Sigma(1385)^+$ signal above a large combinatorial background. Similarly, a $\Sigma(1385)^-$ signal accompanied by a residual Ξ^- peak can be seen in figure 6. Finally, a $\Xi(1530)^0$ peak is observed in figure 7.

The function [28] used to describe the background shape is:

$$N \cdot (m - m_0)^a \cdot \exp(b(m - m_0) + c(m - m_0)^2) ,$$

where m is the invariant mass measured in GeV, m_0 is the kinematic threshold, and N , a , b , and c are constants determined from the fit. For the signal shapes a relativistic Breit-Wigner function with a mass dependent width [29] convolved with a Gaussian to describe the mass resolution was used. Additionally, for the $\Lambda\pi^-$ distribution, a Gaussian for the residual $\Xi^- \rightarrow \Lambda\pi^-$ peak was included. The mass values of the Breit-Wigner functions were free parameters in the fits, while the widths Γ_0 were set to the world average values of 35.8 MeV for the $\Sigma(1385)^+$, 39.4 MeV for the $\Sigma(1385)^-$, and 9.1 MeV for the $\Xi(1530)^0$ [19]. The widths were held fixed since the signals were in many cases close to the turning points of the background shapes and therefore the fits tended to become unstable if the widths were left as free parameters. The fitted values of the central mass values of the peaks were consistent with the world averages [19] associated, however, with large errors. The numbers of $\Sigma(1385)^\pm$ signal events above background within an invariant mass range of 1340 – 1420 MeV were 8563 $\Sigma(1385)^+$ and 8591 $\Sigma(1385)^-$ over backgrounds of 115 758 and 113 521, respectively. For the $\Xi(1530)^0$, 565 signal events were found in the region between 1510 – 1550 MeV over a background of 1 131.

As a cross-check of the background determination method, the number of Ξ^- baryons in the fitted $\Lambda\pi^-$ invariant mass spectrum was extracted. A production cross-section for the Ξ^- was determined from these events and compared to the precise Ξ^- measurement of Section 3.2. The good agreement within statistical errors gave further confidence in the background determination for the resonant baryon states.

3.5 The Orbitally Excited Baryon $\Lambda(1520)$

The $\Lambda(1520)$ was not included in our previous publication [9] and is presented here for the first time. All pairs of oppositely charged tracks used in the fit for the primary vertex were combined and their invariant mass calculated assuming a pK^- combination.

The tracks were required to have at least 20 hits useful for the dE/dx measurement and a p_t of at least 100 MeV. The two tracks were further restricted to originate from the primary vertex by requiring that the $|d_0|$ of both be less than 2 mm. In order to eliminate the background from photon conversions, the invariant mass assuming the tracks to be an electron-positron pair was required to be greater than 150 MeV. The dE/dx particle identification probability was used to reduce the large combinatorial background. The proton (kaon) candidate was required to have a proton (kaon) probability of at least 5%, and kaon (proton) and pion probabilities of less than 5%. Proton-kaon combinations with very low energies ($x_E < 0.035$), very high energies ($x_E > 0.5$), and candidates in the range $0.06 < x_E < 0.10$, where dE/dx particle identification is difficult due to ambiguities between different species, were rejected. The resulting pK^- mass distribution is shown in figure 8, in which a clear $\Lambda(1520)$ peak can be seen.

To confirm that the observed peak was not due to the reflection of a light meson decay, such as $\rho(770)^0 \rightarrow \pi^+\pi^-$, $K_S^0 \rightarrow \pi^+\pi^-$, $K^*(892)^0 \rightarrow K^\pm\pi^\mp$, or $\phi(1020) \rightarrow K^+K^-$, we studied the reflections in the JETSET Monte Carlo events with full detector simulation and found no source which could be responsible for the observed peak. The Monte Carlo background is also shown in figure 8. Note that the $\Lambda(1520)$ is not present in the Monte Carlo simulation, except for a negligible number from decays of heavy flavour hadrons in the JETSET 7.4 events, which had updated decay branching ratios. We confirmed that the observed signal in the data was

stable with respect to variations in selection criteria, the particle identification probability cuts in particular. A clear signal was seen for a wide range (1% to 50%) of the dE/dx probability cuts.

The background under the signal was determined by a fit to the same background function as was applied for the decuplet baryons $\Sigma(1385)^\pm$ and $\Xi(1530)^0$. For the signal shape we used a relativistic D-wave Breit-Wigner function with a mass dependent width [29] in which the central mass value was a free parameter and Γ_0 was set to the world average value of 15.6 MeV [19]. In addition, the signal shape was convolved with a Gaussian to describe the mass resolution, which had an average value of 3 MeV in the Monte Carlo over the observed x_E ranges. The fit range was taken from threshold up to an invariant mass of 1.9 GeV. In the invariant mass region between 1500 and 1540 MeV, a total of 878 signal events were found above a background of 6 804 events.

4 Systematic Errors

In this section we discuss the systematic errors of the baryon measurements. Careful attention has been paid to sources of error which are dependent on x_E and affect the shape of the measured differential cross-section, and those which are global errors that affect only the overall normalisation (details are given in the Appendix). The total systematic errors were obtained by summing in quadrature all of the different systematic errors due to various sources. The results are summarised in table 1 for the total rates and in tables 2–7 for the differential cross-sections.

4.1 Background Determinations

Errors due to the background determinations are given in this section, and are also listed in table 1 under “background” for all of the strange baryons.

The uncertainty in the background subtraction for Λ method 1 was determined by varying the fit range and by using a sideband subtraction as was used in method 2. A systematic error of 1.9% on the Λ rate and an error of 4.9% for individual x_E ranges were obtained. For Λ method 2, the uncertainty due to background subtraction was determined from the uncertainty in the 20% correction factor for the sideband method. The error in the correction factor was taken from Monte Carlo and was determined to be 1.6% overall and 2.4% for individual x_E ranges. In addition, no significant differences were found between JETSET 7.3 and JETSET 7.4.

The systematic errors due to the background determination of the Ξ^- in each x_E bin and the Ω^- were estimated by the statistical error in the factor used to scale the wrong charge combinations. This resulted in 1.2% and 2.0% systematic errors in the total Ξ^- and Ω^- rates, respectively.

For the baryons $\Sigma(1385)^\pm$, $\Xi(1530)^0$, and $\Lambda(1520)$, the systematic errors due to the background determination were estimated by varying the fit ranges and fitting functions. This resulted in overall systematic errors of 1.5%, 1.6%, 1.8%, and 1.8% on the total $\Sigma(1385)^+$, $\Sigma(1385)^-$, $\Xi(1530)^0$, and $\Lambda(1520)$ rates, respectively, and 4.8%, 4.7%, 5.6%, and 5.8%, respectively, for individual x_E ranges.

4.2 Signal Mass Resolution

The mass resolution of the signal affects the efficiency calculation. Disagreement with the data will cause the Monte Carlo to underestimate or overestimate the efficiency, since more or fewer

events will be found outside the signal regions.

The mass resolution of the Λ signal (method 1) is underestimated in the Monte Carlo simulation. The resulting uncertainty in the Λ signal was obtained by varying the interval around the Λ mass peak used for determining the number of reconstructed Λ baryons. The resulting error is 0.6% on the total Λ rate and 1.3% in each x_E range.

As was mentioned previously, the best mass resolution was obtained when both tracks have θ -measurements in either the z -chambers or the endcap. A slightly worse resolution with larger non-Gaussian tails was obtained for the other classes, where none of the tracks or only one of the two tracks has such a measurement, as was allowed for method 2. The Λ mass resolution increased almost linearly with momentum and was larger by approximately 0.5 MeV in the data than in the Monte Carlo for each of the different classes, resulting in an extra loss in efficiency because more events were reconstructed outside the signal region. This extra loss in efficiency has been studied with the Monte Carlo and was found to be proportional to the resolution, reducing the efficiency of finding a Λ by 6.5% for every 1 MeV difference in the mass resolution. Therefore, the efficiency in the Monte Carlo was corrected downwards by 3.25%, with a relative systematic error of 1.7% for the total rate and 3.4% in each x_E range. Since the primary effect of not requiring z -chamber hits for the tracks was to worsen the overall mass resolution, the different z -chamber matching efficiencies in the data and in the Monte Carlo were taken into account by this correction as well.

For the other baryons which decay to final states with a Λ , this systematic error was also added. Additional systematic errors due to the reproduction of the mass resolutions of the other baryons themselves were also considered. These additional errors were estimated by varying the signal regions according to how well the Monte Carlo reproduced the mass resolution. The Ξ^- mass resolution of 5.1 ± 0.2 MeV, was found to be consistent in the data and Monte Carlo. The width of the signal region was varied by ± 2 MeV and the observed variations in the number of signal events found to result in a systematic error of 0.2% overall for the total rate, and 1.0% in each x_E range, giving a total error due to all mass resolution effects including the Λ of 1.7% overall and 3.5% in each x_E range.

The mass resolution of the Ω^- signal is worse in the data (9.0 ± 1.4 MeV) than in the Monte Carlo samples (6.4 ± 0.5 MeV). We studied the effect of this worse resolution by widening the signal region to ± 25 MeV around 1672 MeV and observing that the number of signal events changed by only 2.8%, which was taken as the systematic error due to the Ω^- mass resolution, resulting in a 3.3% systematic error due to all mass resolution effects once the Λ was also taken into account.

For the $\Sigma(1385)^\pm$ and $\Xi(1530)^0$, the systematic errors due to mass resolution effects were dominated by the Λ mass resolution uncertainty. The systematic errors due to the resolution of the $\Sigma(1385)^\pm$, $\Xi(1530)^0$, and $\Lambda(1520)$ signals themselves were estimated by not including the convolution of the Gaussian resolution with the Breit-Wigner resonance and observing the changes in the number of signal events, which are of the order of 0.3 – 0.5% overall and 1% in each x_E interval. The final results for the total production rates are summarised in table 1 under “mass resolution”.

4.3 Simulation of Cut Distributions

The systematic uncertainty due to differences in the resolution of cut distributions between the data and the detector simulation was determined by varying the selection cuts and by comparing different distributions of variables in the data and the Monte Carlo. In particular

the cuts on the impact parameter $|d_0|$, the distance between the intersection point and the first measured hit of the tracks ΔR , the angle Φ , and the required dE/dx measurement were varied. The total Λ rate using method 1 was reproduced to within 1.5% and 4.3% in each x_E bin when $|d_0|$ was varied over the range from 2 mm to 6 mm, ΔR from 1 cm to 9 cm, and Φ from 20 mrad to 100 mrad. In addition, the cuts on the dE/dx measurements were tightened or not required at all. For the other baryons, the same procedure was followed, resulting in errors for Λ method 2 of 2.1% overall and 4.6% in each x_E range. Similar errors were found for the other baryons, and are summarised in table 1 under “cut simulation”.

For the $\Lambda(1520)$, the efficiency of the dE/dx selection for protons was checked directly with the data by measuring the effects of the cuts on protons in $\Lambda \rightarrow p\pi^-$ decays which took place before the inner radius of the jet chamber. Good agreement between data and Monte Carlo was found over the entire momentum range for the proton identification efficiency. A 5.0% systematic error on the rate and 6.2% in each x_E range was assigned due to this source only, yielding 5.4% overall for the cut simulation and 7.7% in each x_E interval.

4.4 x_E Range Correction

In order to calculate the integrated production rates for baryons, we corrected for the unobserved momentum regions. To determine this fractional correction, we relied on the JETSET 7.3 prediction for the Λ (method 1) and JETSET 7.4⁷ for the other baryons. To determine the systematic errors of this extrapolation, half of the difference between the predictions for the fractional correction of JETSET and HERWIG 5.6 was taken.

This results in a systematic error of 0.2% on the measured Λ rate due to the correction, which itself yields about 3% of the total Λ rate. The results for the Λ as well as for the other strange baryons are summarised in table 1 under “ x_E extrapolation”. In the case of the $\Lambda(1520)$, for which the Monte Carlo makes no predictions, the $\Sigma(1385)^\pm$ shape from JETSET 7.4 was taken for the correction and the systematic error was estimated by the difference one obtains if the $\Xi(1530)^0$ shape is used instead.

Due to low statistics, no cross-section as a function of x_E can be extracted for the Ω^- and therefore the shape of the x_E distribution is unknown. We estimated the systematic error due to the assumption that the momentum spectrum is well-modelled by JETSET 7.4 and can be used for the integration of the differential cross-section, by determining the Ξ^- rate in this manner. A 2.3% shift results, which is taken as the systematic error on the Ω^- rate due to the modelling of the fragmentation function.

4.5 Breit-Wigner Resonance Tails

In calculating the cross-sections for resonant states, a correction must be made for the tails of the Breit-Wigner resonance shape. In principle, the tails extend out to the kinematic limits; however, it is not known whether the shape of the resonance at very high masses is well described by a simple Breit-Wigner shape, since the production rate may very well depend on the mass. Furthermore, as the mass becomes very large, so does the mass dependent width [29].

In calculating the cross-sections, a correction was made for extrapolating the signal out to $\pm 4\Gamma_0$ or the kinematic limit, whichever was smaller, as in [18] and [30]. A systematic error

⁷For this correction, we used JETSET with its default parameter tuning. The OPAL tune has baryon fragmentation functions which are harder than in the default JETSET, which is itself too hard, as seen in Section 6.1 below.

equal to half of the difference extrapolating out to 1.9 GeV for the $\Lambda(1520)$ and to 1.8 GeV for the other resonant states was assigned due to the uncertainty in the line shape far from the peak. This results in an average systematic error of about 3% for the total production rates of the different resonances. The results are summarised in table 1 under “Breit-Wigner extrapol.”.

4.6 Other Sources

Another source of systematic uncertainty arises from the finite Monte Carlo statistics used to determine the selection efficiencies. These errors are calculated separately for each x_E range and are included in tables 2–7. The errors on the total rate are given in table 1 under “MC statistics”. For the $\Lambda(1520)$, which is not present in the Monte Carlo samples, protons and kaons which came directly from the fragmentation were paired and weighted so as to reproduce a relativistic Breit-Wigner shape with the correct mass and width. We then studied the effects of the selection cuts on these pairs to determine the efficiency.

Uncertainties in measured branching ratios (taken from [19]) result in some uncertainty in the total production rates, and are given in table 1 under “branching ratios”. In addition, the uncertainty in the efficiency of the multihadronic event selection results in a 0.4% overall systematic error for each baryon, listed in table 1 under “ Z^0 event selection”.

In estimating the systematic error for the efficiency determinations, an additional uncertainty due to the choice of the fragmentation model has not been included, since the effect of this has been taken into account in the “cut simulation” error. The HERWIG 5.6 generator, which provides an alternative fragmentation model, fails to predict the differential cross section of the Λ . There is also a 5% relative difference in the detection efficiency for Λ method 1 when determined with HERWIG 5.6 instead of JETSET 7.3. This is mainly due to differences in the spectra of generated Λ baryons and in the spectrum of particles decaying into the Λ . HERWIG 5.6 predicts too high a rate of Λ from the decays $\Xi \rightarrow \Lambda\pi$ and $\Sigma(1385) \rightarrow \Lambda\pi$. Furthermore, studies of strange particle correlations [10, 31] indicate that HERWIG 5.6 does not model the dynamics of strange particle production as well as JETSET. For these reasons no systematic error arising from differences of fragmentation models was considered. For the other baryons, it was verified that no significant difference in the reconstruction efficiency for different JETSET versions was observed.

5 Cross-section Results

We have estimated the selection efficiencies from the Monte Carlo sample of JETSET 7.3 and JETSET 7.4 events with full detector simulation. For Λ method 1 only the Monte Carlo version JETSET 7.3 was used, since only the data up to and including 1993 are used in the analysis. The JETSET 7.4 events on the other hand were generated using the 1994 detector configuration. After all corrections were made the resulting efficiencies were used to determine the differential cross sections as a function of x_E and $\xi \equiv \ln(1/x_p)$. The total production rates per multihadronic Z^0 decay were then obtained by integrating the differential cross-section and correcting for the unobserved momentum regions.

Differential cross-sections were obtained for Λ , Ξ^- , $\Sigma(1385)^+$, $\Sigma(1385)^-$, $\Xi(1530)^0$, and $\Lambda(1520)$. For the weakly decaying states, the cross-sections include the production from decays of heavier states, such as $\Xi \rightarrow \Lambda\pi$ for example. The results are presented in tables 2–7 and summarised in figures 9 and 10, where the points are plotted at the values given in the tables, determined using the method given in [32]. For the resonant baryons, the endpoints of the

bins in ξ coincided with those in x_E for the central mass value of the resonance. As can be seen in figure 9, the $\Sigma(1385)^\pm$ fragmentation function shape describes the $\Lambda(1520)$ momentum spectrum well, justifying its use in extrapolating to the unobserved momentum regions. As a cross-check of the Λ reconstruction, a cross-section was extracted for method 2 and found to agree very well with that of method 1 within relative systematic errors. No significant deviations were found over the entire x_E range, and the integrated rates of the two determinations agreed.

The total Ω^- efficiency (which is not given in any table) was found to be $(8.9 \pm 0.7)\%$ for the decay sequence $\Omega^- \rightarrow \Lambda K^-$, $\Lambda \rightarrow p\pi^-$, where the error is from Monte Carlo statistics. Since the low statistics did not allow us to divide the signal into finer x_E ranges, only a total rate was determined.

Integrating the differential cross-sections (except for the Ω^-) as described previously, we obtain total production rates of :

$$\begin{aligned}
&0.374 \pm 0.002 \pm 0.010 \Lambda; \\
&0.0259 \pm 0.0004 \pm 0.0009 \Xi^-; \\
&0.0239 \pm 0.0009 \pm 0.0012 \Sigma(1385)^+; \\
&0.0240 \pm 0.0010 \pm 0.0014 \Sigma(1385)^-; \\
&0.0213 \pm 0.0021 \pm 0.0019 \Lambda(1520); \\
&0.0068 \pm 0.0005 \pm 0.0004 \Xi(1530)^0; \text{ and} \\
&0.0018 \pm 0.0003 \pm 0.0002 \Omega^-
\end{aligned}$$

per hadronic Z^0 decay, where the first errors are statistical and the second systematic.

In general the agreement with our previously published results is good. The $\Sigma(1385)^+$ and $\Sigma(1385)^-$ rates are now calculated separately due to an improved background determination. The combined $\Sigma(1385)^+$ and $\Sigma(1385)^-$ rate is:

$$0.0479 \pm 0.0013 \text{ (stat)} \pm 0.0026 \text{ (syst)}$$

per hadronic Z^0 decay, where we have taken into account the correlated systematic errors. The only rates which have changed by more than two standard deviations due to improvement of the simulation and the larger data sample are the Ξ^- and the Ω^- . Previously we measured $0.0206 \pm 0.0011 \text{ (stat)} \pm 0.0019 \text{ (syst)} \Xi^-$ and $0.0050 \pm 0.0012 \text{ (stat)} \pm 0.0009 \text{ (syst)} \Omega^-$ per hadronic Z^0 decay. The latter measurement was based on only 47 ± 11 events. The rates changed mostly because of improvements in the background determinations and statistical fluctuations in the case of the Ω^- . The new results are also consistent with recent measurements by other LEP collaborations [33,34].

At this point it is interesting to compare the production rates with those of other LEP experiments and with data from lower energies. In table 8 are listed the results presented here and in [6,20,30], the published production rates from the other LEP experiments [8,10–12,33–36], and the average production rates from the continuum with $\sqrt{s} \approx 10$ GeV as calculated in [19]. In general good agreement between the various LEP experiments is found. All of the baryon production rates with the exception of the Δ^{++} are generally consistent. Our $\Xi(1530)^0$ production rate is slightly higher than that measured by DELPHI [33]. It is also interesting to note that the OPAL production rates, when compared to the average values at $\sqrt{s} \approx 10$ GeV, are consistent with a simple scaling of the production rates by a factor of 4.1 ± 0.2 with a χ^2 of 8.7 for 8 degrees of freedom.

6 Comparison with Monte Carlo Models and QCD Predictions

In this section we compare the results of the differential cross-sections and integrated production rates with several models and QCD calculations.

6.1 Comparison of Differential Cross-sections

We have already shown that the JETSET Monte Carlo model does not reproduce the shape of the proton [6], Λ [9] and Δ^{++} [30] momentum spectra. Figure 9 shows that the differential cross-sections for Λ and Ξ^- are too hard in JETSET 7.4 (with default parameters, as was used for the x_E extrapolation). The fragmentation function of the $\Lambda(1520)$ is consistent with both the $\Sigma(1385)^\pm$ and $\Xi(1530)^0$ shapes, indicating that orbitally excited baryons have momentum spectra similar to those of $L = 0$ baryons. The HERWIG generator fails to describe the differential cross-sections.

QCD calculations based on the modified leading log approximation (MLLA) [37] predict the shape of the $\xi \equiv \ln(1/x_p)$ distribution for soft gluons, which can be directly compared to the observed hadron spectra under the assumption of local parton hadron duality (LPHD) [38]. This ξ distribution is expected to be approximately Gaussian in shape [39] with the peak shifted to lower values for more massive particles. Such a shape has already been observed at lower centre-of-mass energies [40]. Measurements of inclusive charged particles (predominantly charged pions) at the Z^0 pole are well described by such a distribution with a peak at about $\xi_{max} = 3.65$ [41]. We have already shown that identified mesons and baryons at the Z^0 pole exhibit a shift of the maximum to lower values for heavier masses [6, 9, 13, 16]. From our measured differential cross-sections, plotted as a function of ξ (figure 10), we have determined ξ_{max} by fitting a Gaussian to the ξ distributions and find:

$$\begin{aligned}\xi_{max}(\Lambda) &= 2.75 \pm 0.05 \quad (2.52); \\ \xi_{max}(\Xi^-) &= 2.72 \pm 0.13 \quad (2.28); \\ \xi_{max}(\Sigma(1385)^+) &= 3.04 \pm 0.38 \quad (2.28); \\ \xi_{max}(\Sigma(1385)^-) &= 3.04 \pm 0.37 \quad (2.46); \\ \xi_{max}(\Lambda(1520)) &= 1.89 \pm 0.60 \quad (\text{no prediction}); \\ \xi_{max}(\Xi(1530)^0) &= 2.42 \pm 0.14 \quad (2.34),\end{aligned}$$

where the JETSET 7.4 predictions are given in parentheses. The values of ξ_{max} are in general agreement with the hypothesis that the peak position of the ξ distribution decreases with increasing hadron mass. However, the peak position can be shifted by contributions from decays as was shown in [8, 16]. In particular, $\xi_{max}(\Lambda)$ and $\xi_{max}(\Xi^-)$ are shifted upwards in JETSET 7.4 by as much as 10% due to a softening of the momentum spectra by resonance decays such as $\Sigma(1385) \rightarrow \Lambda\pi$ and $\Xi(1530) \rightarrow \Xi\pi$. The fact that the JETSET 7.4 predicted ξ_{max} values are all low with respect to the data indicates that baryon momentum spectra are generally too hard in JETSET.

6.2 Comparison of Total Rates

It is to be noted that neither the JETSET nor the HERWIG Monte Carlo models consider excited $L \neq 0$ baryon production. Given the significant production rate of the $\Lambda(1520)$, which

is comparable to the production rates of the $J^P = \frac{3}{2}^+$ decuplet baryons already measured, it would seem plausible that the production of such resonances would influence the lighter baryon rates through a feed-down effect. Caution must therefore be exercised when comparing measured inclusive particle production rates with models, since hadronisation model predictions should ideally be compared at the level of the directly produced states⁸.

Nevertheless one can argue for the moment that spin $\frac{3}{2}$ baryons are for the most part direct, as they are currently modelled in JETSET and HERWIG. Our $\Lambda(1520)$ rate is comparable to the rates of the $\Sigma(1385)^+$ and $\Sigma(1385)^-$, baryons with the same total spin and strangeness as the $\Lambda(1520)$. This is consistent with what has been measured at lower energies [18]. On the other hand the $\Lambda(1520)$ rate is found to be significantly higher than the production rate of the $\Xi(1530)^0$, a baryon with similar mass and total spin, but different strangeness.

We have also compared the inclusive production rates with the JETSET Monte Carlo to test the diquark model of baryon production. According to this model several parameters determine the various production yields. These include:

- the diquark to quark (qq/q) production ratio, **PARJ(1)**;
- the strange to non-strange quark production ratio, $\gamma_s/\gamma_u = \gamma_s/\gamma_d = \mathbf{PARJ(2)}$;
- a parameter for extra suppression of strange quarks in a diquark (us/ud)/(s/d), **PARJ(3)**;
- a parameter to suppress spin 1 diquarks relative to spin 0 diquarks $\frac{1}{3}(\mathbf{qq_1}/\mathbf{qq_0})$, **PARJ(4)**;
and
- the popcorn parameter, **PARJ(5)**.

The diquark to quark ratio regulates the production of diquarks from the sea, thus affecting most baryon production rates in the same way, and determines the overall baryon/meson ratio. The strange to non-strange quark production ratio determines how often a strange quark-antiquark pair is produced from the sea, and therefore affects all strange hadron production (including kaon production, for example). It is a general assumption of hadronisation that u and d quarks are produced from the sea with approximately equal probabilities, while strange quarks are suppressed due to their larger mass and have relative production probabilities of approximately $\gamma_s/\gamma_u \approx \gamma_s/\gamma_d = 0.29 \pm 0.015$ [42]. In QCD, SU(2) isospin invariance under the exchange of u and d quarks is an approximate symmetry which arises from the flavour independence of QCD and the nearly degenerate u and d quark masses. It is therefore interesting to note that the production rates of $\Sigma(1385)^+$ and $\Sigma(1385)^-$ are consistent:

$$\Sigma(1385)^+/\Sigma(1385)^- = 1.00 \pm 0.06 \text{ (stat)} \pm 0.01 \text{ (syst)} ,$$

where the systematic error is due only to Monte Carlo statistics since the other systematic errors cancel in the ratio. This supports the hypothesis that $\gamma_u \approx \gamma_d$. Note that this ratio in JETSET 7.4 is equal to 1.06 due to different branching ratios of the $\Lambda_c^+ \rightarrow \Sigma(1385)^+$ and $\Lambda_c^+ \rightarrow \Sigma(1385)^-$. The extra suppression of strange quarks in a diquark is introduced because of the measured low Ξ^-/Λ ratio, for example. The suppression of spin 1 diquarks takes into account the lower production rates of the heavier $J^P = \frac{3}{2}^+$ decuplet baryons. Finally an extension of the diquark model, called the popcorn mechanism [43], is introduced by including the possibility of producing additional mesons between the baryon-antibaryon pair.

⁸Directly produced hadrons are those which come directly from the fragmentation and not from secondary decays of long-lived states, although the definition of “long-lived” is open to some interpretation.

We previously demonstrated [9] that no tuning of JETSET could give a satisfactory description of all of the decuplet baryons measured. In order to make more direct comparisons between the data and the models, it is instructive to calculate ratios of baryon production rates. These ratios allow the comparison of baryons with different spins and strangeness, with the advantage that common systematic errors (such as that for the Λ mass resolution) cancel. We compare the measured rates with the results of the default version of JETSET 7.4 (with no tuning to OPAL event shapes, etc.) in table 9. The predictions of JETSET 7.3 are rather similar (see also table 9) and do not affect the conclusions in what follows. The HERWIG 5.6 predictions⁹ are also given in table 9. We determined the following ratios of octet baryon production rates:

$$\begin{aligned}\Lambda/p &= 0.41 \pm 0.05 \quad (0.32); \\ \frac{1}{3}[\Sigma^+ + \Sigma^0 + \Sigma^-]/p &= 0.091 \pm 0.015 \quad (0.059); \\ \Xi^-/\Lambda &= 0.069 \pm 0.003 \quad (0.071); \end{aligned}$$

where the JETSET 7.4 predictions are given in parentheses, and we have used the measurements from [6,20]. These ratios are sensitive to strangeness suppression in diquarks, which is controlled by two parameters, the (s/d) strangeness suppression and the extra strangeness suppression in diquarks (us/ud)/(s/d). From these ratios, and using the measured kaon rates at LEP, one can fix the strangeness suppression parameters for both single quarks and diquarks to obtain reasonable agreement with the data.

We have also calculated ratios of the decuplet baryons, which are thought to be less influenced by feed-down effects from decays:

$$\begin{aligned}\Sigma(1385)^+/\Delta^{++} &= 0.11 \pm 0.03 \quad (0.20); \\ \Sigma(1385)^-/\Delta^{++} &= 0.11 \pm 0.03 \quad (0.19); \\ \Xi(1530)^0/\Sigma(1385)^+ &= 0.28 \pm 0.03 \quad (0.14); \\ \Xi(1530)^0/\Sigma(1385)^- &= 0.28 \pm 0.03 \quad (0.15); \\ \Omega^-/\Xi(1530)^0 &= 0.26 \pm 0.06 \quad (0.13); \end{aligned}$$

where we have included the OPAL Δ^{++} measurement from [30]. Rather poor agreement with JETSET 7.4 (given in parentheses) is found for the ratios of decuplet baryons. The parameters which influence these production rates are the spin 1 diquark suppression parameter (which scales all of the above ratios in a similar manner), the strangeness suppression parameters (which have been already fixed by the measurements of the octet baryons), and the popcorn probability. Since the first two ratios are too high in the Monte Carlo, while the others are too low, and since any parameter change shifts all of the above ratios up or down in the same direction, it is clear that no tuning can reach overall agreement. Therefore, the decuplet baryon production rates can not be described by a single tuning parameter for spin 1 diquarks. In addition, complementary studies by OPAL have been made which use the recent measurements of the $J^P = \frac{1}{2}^+ \Sigma$ baryons [20] which indicate deficiencies in the way strangeness suppression is currently implemented for baryons in JETSET.

It should be noted that the model does not include the production of orbitally excited baryons, which might improve the agreement. The observation of a significant production rate

⁹In order to achieve better agreement with general event shapes and LEP average hadron production rates, OPAL have tuned the maximum cluster mass parameter from the default of 3.5 GeV to 2.8 GeV and the power in the maximum cluster mass parameter from 2 to 1.22.

for the $\Lambda(1520)$ demonstrates that the production cross-sections of orbitally excited baryons are not negligible.

Finally, we have compared the inclusive measured baryon yields with the predictions of a thermodynamic model of baryon production [44], which assumes that baryon rates are determined by their mass and spin in a statistical way, and which can describe hadron production in terms of relatively few parameters. The predictions of this model are given in table 9 and are seen to be in reasonable agreement with the data, including the $\Lambda(1520)$. The predicted Λ rate is low compared to the data. However, it is strongly correlated to the $\Sigma(1385)$ rate. If one removes the $\Sigma(1385)$ rate from the fit, a higher Λ rate consistent with LEP measurements is obtained. Another recent calculation [45] describes the production of light flavoured hadrons based on the idea of string fragmentation. Reasonable agreement is found for many particle yields.

7 Summary

We have measured the differential cross-sections as functions of the scaled energy x_E and $\ln(1/x_p)$ for the following strange baryons: Λ , Ξ^- , $\Sigma(1385)^+$, $\Sigma(1385)^-$, $\Xi(1530)^0$, and the orbitally excited state $\Lambda(1520)$. The differential cross-sections as a function of x_E , the scaled energy, of Λ and Ξ^- baryons were found to be softer than those predicted by the JETSET and HERWIG Monte Carlo generators. Comparisons of the momentum spectra of several strange baryons with the predictions of an analytical QCD formula show the expected mass dependence of the peak of the $\xi = \ln(1/x_p)$ distributions.

Total production rates have been obtained by integrating the differential cross-sections and correcting for the unobserved x_E ranges. In addition an Ω^- rate has been measured, although the low statistics preclude a measurement of the fragmentation function. From our measurements, we conclude that the measured baryon yields disagree with the simple diquark picture, as implemented in JETSET, in which only one tuning parameter for spin 1 diquarks is used. Similar problems with strangeness suppression in baryons as implemented in JETSET were found in a complementary analysis of the $J^P = \frac{1}{2}^+$ states Σ^+ , Σ^0 , and Σ^- [20]. The HERWIG Monte Carlo, with fewer free parameters, was unable to reproduce either the octet or decuplet baryon rates. A comparison of the data with a thermodynamic model of hadron production which includes orbitally excited meson and baryon states showed reasonable agreement.

The $\Lambda(1520)$ (and other excited baryon states) are noticeably absent from JETSET and HERWIG. A more detailed treatment of spin effects such as the inclusion of excited states and more fundamental treatments of correlations such as those due to the Bose-Einstein effect would be welcome additions, and would hopefully improve the agreement of the models with the measurements.

Appendix on Systematic Errors

This Appendix summarises the method used to determine the systematic errors which affect the overall normalisation of the cross-section and those which affect the point-to-point behaviour of the differential distribution.

To estimate the systematic error of a measured distribution, $N_0(k)$, which is divided into bins $k = 1, \dots, n$, the procedure to determine $N_0(k)$ is usually repeated with various modifications, such as varying the selection criteria and cuts, using different methods to estimate background, etc. Usually the results in each bin are not exactly reproduced and it has to be estimated if these deviations are compatible with statistical fluctuations or indicate a systematic effect. A possible systematic uncertainty can be factored into two independent parts, one giving an overall normalisation error, and the other a bin-by-bin error which represents the range in which the differential distribution can be distorted without affecting the integrated result.

To obtain these errors, the following procedure has been applied. Consider the distribution $N_0(k) = N_0(k, a)$ in bins $k = 1, \dots, n$. The number of entries m_k in each bin k depends on some quantity a , for example a cut on the minimum number of hits required for a track to be considered for the measurement. The systematic uncertainty due to this parameter a is then studied by varying the cut value. A variation of the parameter $a_1 = a + \Delta a$ yields another distribution

$$N_1(k) = N_0(k, a_1)$$

and the ratio

$$R_1(k) = N_1(k)/N_0(k)$$

with a statistical error

$$\Delta R_1(k) = \Delta N_1(k)/N_0(k)$$

The overall normalisation error and the bin-by-bin error can then be found by superimposing n Gaussian functions with weights m_k , centroids $R_1(k)$, and standard deviations $\Delta R_1(k)$. To the resulting (nearly) Gaussian-shaped distribution a Gaussian which has a mean $\langle R_1 \rangle$ and a standard deviation $\sqrt{v_1}$ can be fitted. The parameter v_1 contains a contribution from the systematic error and another from the statistical error. The latter can be unfolded by

$$v_1^{sys} = v_1 - v_1^{stat}.$$

The variance v_1^{stat} of the statistical error is calculated in a similar way to v_1 with N_0 replacing N_1 in R_1 . Thus, statistical and systematic errors are treated in the same manner. The meaning of the systematic errors obtained is:

$$\begin{aligned} \langle R_1 \rangle &= \text{correction factor on the overall normalisation} \\ \sigma_1^{sys} = \sqrt{v_1^{sys}} &= \text{bin-by-bin error giving the limit within which the shape of the} \\ &\quad \text{distribution } R_1 \text{ may change without affecting the overall normalisation.} \\ &\quad \text{A hypothetical distribution, normalised to the data, is consistent at the} \\ &\quad \text{one standard deviation level with the measured distribution if its rms} \\ &\quad \text{deviation from the observed data, averaged over all bins, is less than the} \\ &\quad \text{bin-by-bin error.} \end{aligned}$$

This procedure may then be repeated with:

- several variations a_i , $i = 1, \dots, m$ of the same parameter (or cut) a , in which case the systematic errors have to be averaged, or
- variation of different independent parameters (or cuts) one at a time, a, b, c, \dots , in which case the errors have to be added in quadrature.

Note that if a theoretical description of the distribution $N_0(k)$ had been available, the procedure could have been performed with the theoretical values in place of $N_0(k)$. The reliability of this procedure for deriving overall normalisation and bin-by-bin errors has been verified for various simple models.

The systematic errors obtained can be compared to the more common approach of “conservative estimates”, which take, for example, half the difference between two results measured with and without some modification in the procedure. These latter errors are somewhat arbitrary and do not consider differences due to statistical fluctuations. If, however, the average point-to-point systematic error of the Λ differential cross-section calculated as described previously is compared to the “conservative estimates” of individual bin-by-bin errors, the latter values are slightly larger (by less than one standard deviation of the statistical error) for very high or very low x_E and slightly smaller for intermediate values.

Acknowledgements:

We particularly wish to thank the SL Division for the efficient operation of the LEP accelerator and for their continuing close cooperation with our experimental group. In addition to the support staff at our own institutions we are pleased to acknowledge the

Department of Energy, USA,

National Science Foundation, USA,

Particle Physics and Astronomy Research Council, UK,

Natural Sciences and Engineering Research Council, Canada,

Israel Ministry of Science,

Israel Science Foundation, administered by the Israel Academy of Science and Humanities,

Minerva Gesellschaft,

Japanese Ministry of Education, Science and Culture (the Monbusho) and a grant under the Monbusho International Science Research Program,

German Israeli Bi-national Science Foundation (GIF),

Direction des Sciences de la Matière du Commissariat à l’Energie Atomique, France,

Bundesministerium für Bildung, Wissenschaft, Forschung und Technologie, Germany,

National Research Council of Canada,

Hungarian Foundation for Scientific Research, OTKA T-016660, and OTKA F-015089.

References

- [1] B. Andersson *et al.*, Nucl. Phys. **B197** (1982) 45.
- [2] B. Andersson *et al.*, Phys. Rep. **97** (1983) 31.
- [3] T. Sjöstrand, Comp. Phys. Comm. **39** (1986) 347;
T. Sjöstrand and M. Bengtsson, Comp. Phys. Comm. **43** (1987) 367;
T. Sjöstrand, Comp. Phys. Comm. **82** (1994) 74.
- [4] G. Marchesini and B.R. Webber, Nucl. Phys. **B310** (1988) 461;
G. Marchesini, B.R. Webber *et al.*, Comp. Phys. Comm. **67** (1992) 465.
- [5] See for example:
D. Saxon, RAL-88-102;
P. Mättig, Phys. Rep. **177** (1989) 141;
G.D. Lafferty, P.I. Reeves, and M.R. Whalley, J. Phys. G: Nucl. Part. Phys. **21** (1995) A1.
- [6] OPAL Collab., R. Akers *et al.*, Z. Phys. **C63** (1994) 181.
- [7] ALEPH Collab., D. Buskulic *et al.*, Z. Phys. **C66** (1995) 355.
- [8] DELPHI Collab., P. Abreu *et al.*, Nucl. Phys. **B444** (1995) 3.
- [9] OPAL Collab., P.D. Acton *et al.*, Phys. Lett. **B291** (1992) 503.
- [10] DELPHI Collab., P. Abreu *et al.*, Phys. Lett. **B318** (1993) 249.
- [11] ALEPH Collab., D. Buskulic *et al.*, Z. Phys. **C64** (1994) 361.
- [12] L3 Collab., M. Acciarri *et al.*, Phys. Lett. **B328** (1994) 223.
- [13] OPAL Collab., R. Akers *et al.*, Z. Phys. **C67** (1995) 389.
- [14] DELPHI Collab., P. Abreu *et al.*, Z. Phys. **C65** (1995) 587.
- [15] HRS Collab. S. Abachi *et al.*, Phys. Rev. Lett. **57** (1986) 1990.
- [16] OPAL Collab., R. Akers *et al.*, Z. Phys. **C68** (1995) 1.
- [17] DELPHI Collab., P. Abreu *et al.*, CERN-PPE/96-26.
- [18] ARGUS Collab., H. Albrecht *et al.*, Phys. Lett. **B215** (1988) 429.
- [19] Particle Data Group, L. Montanet *et al.*, *Review of Particle Properties*, Phys. Rev. **D50** (1994) 1173.
- [20] OPAL Collab., G. Alexander *et al.*, CERN-PPE/96-100.
- [21] OPAL Collab., M. Ahmet *et al.*, Nucl. Instr. and Meth. **A305** (1991) 275.
- [22] P. Allport *et al.*, Nucl. Instr. and Meth. **A324** (1993) 34;
P. Allport *et al.*, Nucl. Instr. and Meth. **A346** (1994) 476.
- [23] M. Hauschild *et al.*, Nucl. Instr. and Meth. **A314** (1992) 74.

- [24] OPAL Collaboration, G. Alexander *et al.*, Z. Phys. **C52** (1991) 175.
- [25] J. Allison *et al.*, Nucl. Instr. and Meth. **A317** (1992) 47.
- [26] OPAL Collaboration, P.D. Acton *et al.*, Z. Phys. **C58** (1993) 387;
OPAL Collaboration, R. Akers *et al.*, Z. Phys. **C69** (1996) 543.
- [27] O. Biebel *et al.*, Nucl. Instr. and Meth. **A323** (1992) 169.
- [28] This functional form was first suggested in:
ALEPH Collab., *Hyperon Production in Z Decays*, Contributed paper to the International
Europhysics Conference on High Energy Physics, Brussels (1995), EPS Ref. EPS-0419.
- [29] J.D. Jackson, Nuovo Cim. **34** (1964) 1644.
- [30] OPAL Collab., G. Alexander *et al.*, Phys. Lett. **B358** (1995) 162.
- [31] OPAL Collab., P.D. Acton *et al.*, Phys. Lett. **B305** (1993) 415.
- [32] G.D. Lafferty and T.R. Wyatt, Nucl. Instr. and Meth. **A355** (1995) 541.
- [33] DELPHI Collab., P. Abreu *et al.*, Z. Phys. **C67** (1995) 543.
- [34] DELPHI Collab., W. Adam *et al.*, Z. Phys **C70** (1996) 371.
- [35] DELPHI Collab., P. Abreu *et al.*, Phys. Lett. **B316** (1993) 253.
- [36] DELPHI Collab., P. Abreu *et al.*, Phys. Lett. **B361** (1995) 207.
- [37] Y.I. Azimov, Y.L. Dokshitzer, V.A. Khoze, and S.I. Troyan, Z. Phys. **C27** (1985) 65;
Y.L. Dokshitzer, V.A. Khoze, and S.I. Troyan, *Perturbative QCD*, ed. A.H. Mueller,
Singapore: World Scientific 1989.
- [38] D. Amati and G. Veneziano, Phys. Lett. **B83** (1979) 87;
Y.I. Azimov, Y.L. Dokshitzer, V.A. Khoze and S.I. Troyan, Phys. Lett. **B165** (1985) 147.
- [39] Y.L. Dokshitzer, V.A. Khoze and S.I. Troyan, J. Phys. G: Nucl. Part. Phys **17** (1991)
1481;
Y.L. Dokshitzer, V.A. Khoze and S.I. Troyan, Z. Phys. **C55** (1992) 107.
- [40] TASSO Collab., M. Althoff *et al.*, Z. Phys. **C22** (1984) 307.
- [41] OPAL Collab., P.D. Acton *et al.*, Z. Phys. **C53** (1992) 539;
OPAL Collab., R. Akers *et al.*, Z. Phys. **C68** (1995) 203.
- [42] G. Bocquet *et al.*, Phys. Lett. **B366** (1996) 447.
- [43] B. Andersson *et al.*, Physica Scripta **32** (1985) 574.
- [44] F. Becattini, Z. Phys. **C69** (1996) 485.
The quoted results were obtained directly from the author.
- [45] Y. Pei, CERN-PPE/96-37.

	Λ_{method1}	Λ_{method2}	Ξ^-	Ω^-
signal events	94877	244415	6736	252
background events	39126	99753	3085	960
background	1.9%	1.6%	1.2%	2.0%
mass resolution	0.6%	1.7%	1.7%	3.3%
cut simulation	1.5%	2.1%	2.8%	2.9%
x_E extrapolation	0.2%	0.2%	0.4%	2.3%
MC statistics	0.3%	0.2%	1.0%	7.6%
branching ratios	0.8%	0.8%	0.8%	1.3%
Z^0 event selection	0.4%	0.4%	0.4%	0.4%
total systematic error	2.6%	3.3%	3.7%	9.4%
statistical error	0.4%	0.3%	1.7%	18.9%

	$\Sigma(1385)^+$	$\Sigma(1385)^-$	$\Xi(1530)^0$	$\Lambda(1520)$
signal events	8563	8591	565	878
background events	115758	113521	1131	6804
background	1.5%	1.6%	1.8%	1.8%
mass resolution	1.8%	1.8%	1.8%	0.5%
cut simulation	2.6%	2.7%	2.9%	5.4%
x_E extrapolation	0.7%	2.0%	2.2%	0.6%
Breit-Wigner extrap.	2.4%	3.2%	3.0%	4.1%
MC statistics	0.6%	0.6%	3.6%	4.7%
branching ratios	2.4%	2.4%	0.8%	2.2%
Z^0 event selection	0.4%	0.4%	0.4%	0.4%
total systematic error	5.0%	5.8%	6.5%	8.8%
statistical error	3.6%	4.3%	7.4%	10.0%

Table 1: Number of observed baryons and the different systematic errors of the measurements.

x_E	$\langle x_E \rangle_{lw}$	n	efficiency	$(1/\sigma_{had})d\sigma/dx_E$
0.027-0.035	0.031	4094 \pm 71	0.074 \pm 0.001	5.64 \pm 0.10 \pm 0.39
0.035-0.045	0.040	9020 \pm 105	0.160 \pm 0.002	4.59 \pm 0.05 \pm 0.31
0.045-0.055	0.050	9257 \pm 125	0.208 \pm 0.002	3.63 \pm 0.05 \pm 0.25
0.055-0.062	0.059	6914 \pm 107	0.258 \pm 0.003	3.11 \pm 0.05 \pm 0.21
0.062-0.070	0.066	7287 \pm 108	0.282 \pm 0.003	2.63 \pm 0.04 \pm 0.18
0.070-0.085	0.077	10729 \pm 124	0.293 \pm 0.003	1.98 \pm 0.02 \pm 0.13
0.085-0.105	0.095	10788 \pm 119	0.302 \pm 0.003	1.452 \pm 0.016 \pm 0.097
0.105-0.120	0.112	6486 \pm 91	0.296 \pm 0.003	1.184 \pm 0.017 \pm 0.080
0.120-0.150	0.135	9180 \pm 110	0.282 \pm 0.003	0.883 \pm 0.011 \pm 0.059
0.150-0.200	0.174	9047 \pm 109	0.252 \pm 0.002	0.585 \pm 0.007 \pm 0.039
0.200-0.300	0.247	7789 \pm 101	0.193 \pm 0.002	0.329 \pm 0.004 \pm 0.022
0.300-0.400	0.347	2673 \pm 59	0.147 \pm 0.002	0.148 \pm 0.003 \pm 0.010
0.400-0.500	0.446	1140 \pm 38	0.108 \pm 0.003	0.086 \pm 0.003 \pm 0.006
0.500-0.600	0.545	370 \pm 23	0.095 \pm 0.004	0.032 \pm 0.002 \pm 0.003
0.600-0.700	0.641	103 \pm 14	0.085 \pm 0.006	0.010 \pm 0.001 \pm 0.001

ξ	$\langle \xi \rangle_{lw}$	efficiency	$(1/\sigma_{had})d\sigma/d\xi$
0.6-0.8	0.72	0.106 \pm 0.004	0.024 \pm 0.001 \pm 0.002
0.8-1.0	0.92	0.119 \pm 0.003	0.040 \pm 0.002 \pm 0.003
1.0-1.2	1.10	0.155 \pm 0.003	0.052 \pm 0.002 \pm 0.004
1.2-1.4	1.30	0.173 \pm 0.003	0.071 \pm 0.002 \pm 0.005
1.4-1.6	1.50	0.207 \pm 0.003	0.087 \pm 0.002 \pm 0.006
1.6-1.8	1.70	0.240 \pm 0.003	0.096 \pm 0.002 \pm 0.007
1.8-2.0	1.90	0.275 \pm 0.003	0.105 \pm 0.002 \pm 0.007
2.0-2.2	2.10	0.287 \pm 0.003	0.120 \pm 0.002 \pm 0.008
2.2-2.4	2.30	0.300 \pm 0.003	0.123 \pm 0.002 \pm 0.008
2.4-2.6	2.50	0.293 \pm 0.003	0.140 \pm 0.002 \pm 0.009
2.6-2.8	2.70	0.292 \pm 0.003	0.141 \pm 0.002 \pm 0.010
2.8-3.0	2.90	0.265 \pm 0.003	0.148 \pm 0.002 \pm 0.010
3.0-3.2	3.10	0.222 \pm 0.002	0.137 \pm 0.003 \pm 0.009
3.2-3.4	3.30	0.175 \pm 0.002	0.127 \pm 0.003 \pm 0.009
3.4-3.6	3.50	0.160 \pm 0.002	0.110 \pm 0.002 \pm 0.008
3.6-3.8	3.70	0.124 \pm 0.002	0.093 \pm 0.003 \pm 0.007
3.8-4.0	3.90	0.092 \pm 0.002	0.074 \pm 0.003 \pm 0.006
4.0-4.2	4.10	0.059 \pm 0.002	0.052 \pm 0.003 \pm 0.004

Table 2: Differential cross-sections for Λ as a function of x_E and $\xi \equiv \ln(1/x_p)$. Given are the statistical and the systematic errors which affect the point-to-point cross-section.

x_E	$\langle x_E \rangle_{lw}$	n	efficiency	$(1/\sigma_{had})d\sigma/dx_E$
0.035-0.050	0.042	474 \pm 25	0.039 \pm 0.001	0.341 \pm 0.018 \pm 0.032
0.050-0.060	0.055	567 \pm 30	0.094 \pm 0.003	0.254 \pm 0.014 \pm 0.021
0.060-0.080	0.070	1312 \pm 49	0.154 \pm 0.003	0.180 \pm 0.007 \pm 0.012
0.080-0.100	0.090	1080 \pm 46	0.201 \pm 0.004	0.114 \pm 0.005 \pm 0.008
0.100-0.150	0.123	1762 \pm 56	0.202 \pm 0.003	0.0737 \pm 0.0024 \pm 0.0048
0.150-0.200	0.172	845 \pm 40	0.163 \pm 0.004	0.0438 \pm 0.0021 \pm 0.0031
0.200-0.300	0.243	466 \pm 35	0.102 \pm 0.003	0.0192 \pm 0.0015 \pm 0.0014
0.300-0.400	0.339	174 \pm 18	0.060 \pm 0.003	0.0120 \pm 0.0012 \pm 0.0012
0.400-0.500	0.434	56 \pm 9	0.028 \pm 0.002	0.0084 \pm 0.0014 \pm 0.0015

ξ	$\langle \xi \rangle_{lw}$	efficiency	$(1/\sigma_{had})d\sigma/d\xi$
0.6-0.8	0.72	0.049 \pm 0.003	0.0026 \pm 0.0005 \pm 0.0017
0.8-1.0	0.92	0.078 \pm 0.004	0.0044 \pm 0.0004 \pm 0.0011
1.0-1.2	1.10	0.100 \pm 0.004	0.0044 \pm 0.0004 \pm 0.0005
1.2-1.4	1.30	0.119 \pm 0.004	0.0050 \pm 0.0005 \pm 0.0005
1.4-1.6	1.50	0.155 \pm 0.004	0.0071 \pm 0.0004 \pm 0.0006
1.6-1.8	1.70	0.197 \pm 0.004	0.0075 \pm 0.0004 \pm 0.0006
1.8-2.0	1.90	0.206 \pm 0.005	0.0088 \pm 0.0004 \pm 0.0007
2.0-2.2	2.10	0.222 \pm 0.005	0.0086 \pm 0.0004 \pm 0.0006
2.2-2.4	2.30	0.199 \pm 0.005	0.0094 \pm 0.0004 \pm 0.0007
2.4-2.6	2.50	0.166 \pm 0.005	0.0103 \pm 0.0005 \pm 0.0008
2.6-2.8	2.70	0.116 \pm 0.004	0.0121 \pm 0.0006 \pm 0.0009
2.8-3.0	2.90	0.085 \pm 0.004	0.0102 \pm 0.0006 \pm 0.0008
3.0-3.2	3.10	0.057 \pm 0.003	0.0100 \pm 0.0007 \pm 0.0009
3.2-3.4	3.28	0.033 \pm 0.003	0.0087 \pm 0.0009 \pm 0.0010
3.4-3.6	3.46	0.016 \pm 0.002	0.0088 \pm 0.0011 \pm 0.0013

Table 3: Differential cross-sections for Ξ^- as a function of x_E and $\xi \equiv \ln(1/x_p)$. Given are the statistical and those systematic errors which affect the point-to-point cross-section.

x_E	$\langle x_E \rangle_{lw}$	n	efficiency	$(1/\sigma_{had})d\sigma/dx_E$	ξ	$\langle \xi \rangle_{lw}$	$(1/\sigma_{had})d\sigma/d\xi$
.04-.07	.054	2676 \pm 188	.193 \pm .003	.280 \pm .020 \pm .021	2.76-3.65	3.21	.0095 \pm .0007 \pm .0007
.07-.10	.084	1866 \pm 182	.320 \pm .004	.118 \pm .012 \pm .009	2.35-2.76	2.55	.0086 \pm .0008 \pm .0007
.10-.15	.124	1684 \pm 162	.329 \pm .004	.0619 \pm .0060 \pm .0047	1.92-2.35	2.13	.0072 \pm .0007 \pm .0005
.15-.20	.173	959 \pm 114	.288 \pm .005	.0403 \pm .0048 \pm .0031	1.62-1.92	1.77	.0068 \pm .0008 \pm .0005
.20-.30	.245	976 \pm 107	.238 \pm .004	.0248 \pm .0027 \pm .0019	1.21-1.62	1.42	.0060 \pm .0007 \pm .0005
.30-.50	.384	402 \pm 71	.161 \pm .003	.0076 \pm .0013 \pm .0006	0.70-1.21	0.96	.0030 \pm .0005 \pm .0002

Table 4: Differential cross-sections for $\Sigma(1385)^+$ as a function of x_E and $\xi \equiv \ln(1/x_p)$. Given are the statistical and those systematic error which affect the point-to-point cross-section.

x_E	$\langle x_E \rangle_{lw}$	n	efficiency	$(1/\sigma_{had})d\sigma/dx_E$	ξ	$\langle \xi \rangle_{lw}$	$(1/\sigma_{had})d\sigma/d\xi$
.04-.07	.054	3021 \pm 188	.184 \pm .002	.291 \pm .021 \pm .022	2.76-3.65	3.21	.0098 \pm .0007 \pm .0007
.07-.10	.084	1971 \pm 182	.303 \pm .004	.116 \pm .013 \pm .009	2.35-2.76	2.55	.0085 \pm .0009 \pm .0006
.10-.15	.124	1718 \pm 162	.283 \pm .004	.0646 \pm .0071 \pm .0049	1.92-2.35	2.13	.0075 \pm .0008 \pm .0006
.15-.20	.173	887 \pm 114	.227 \pm .004	.0414 \pm .0061 \pm .0032	1.62-1.92	1.77	.0070 \pm .0010 \pm .0005
.20-.30	.245	736 \pm 107	.166 \pm .003	.0235 \pm .0040 \pm .0018	1.21-1.62	1.42	.0057 \pm .0010 \pm .0004
.30-.50	.384	258 \pm 71	.111 \pm .003	.0062 \pm .0020 \pm .0005	0.70-1.21	0.96	.0024 \pm .0008 \pm .0002

Table 5: Differential cross-sections for $\Sigma(1385)^-$ as a function of x_E and $\xi \equiv \ln(1/x_p)$. Given are the statistical and those systematic error which affect the point-to-point cross-section.

x_E	$\langle x_E \rangle_{lw}$	n	efficiency	$(1/\sigma_{had})d\sigma/dx_E$	ξ	$\langle \xi \rangle_{lw}$	$(1/\sigma_{had})d\sigma/d\xi$
.04-.07	.054	68 \pm 15	.027 \pm .003	.064 \pm .014 \pm .009	2.79-3.83	3.20	.0019 \pm .0004 \pm .0003
.07-.10	.084	151 \pm 21	.098 \pm .007	.0387 \pm .0054 \pm .0042	2.36-2.79	2.55	.0027 \pm .0004 \pm .0003
.10-.15	.123	198 \pm 23	.126 \pm .008	.0239 \pm .0028 \pm .0024	1.92-2.36	2.13	.0027 \pm .0003 \pm .0003
.15-.20	.173	100 \pm 17	.105 \pm .009	.0144 \pm .0025 \pm .0017	1.62-1.92	1.77	.0024 \pm .0004 \pm .0003
.20-.30	.245	48 \pm 15	.075 \pm .007	.0049 \pm .0015 \pm .0006	1.21-1.62	1.42	.0012 \pm .0004 \pm .0002

Table 6: Differential cross-sections for $\Xi(1530)^0$ as a function of x_E and $\xi \equiv \ln(1/x_p)$. Given are the statistical and those systematic error which affect the point-to-point cross-section.

x_E	$\langle x_E \rangle_{lw}$	n	efficiency	$(1/\sigma_{had})d\sigma/dx_E$	ξ	$\langle \xi \rangle_{lw}$	$(1/\sigma_{had})d\sigma/d\xi$
.035-.039	.037	140 \pm 22	.094 \pm .013	.447 \pm .070 \pm .076	3.90-4.54	4.22	.0026 \pm .0004 \pm .0004
.039-.045	.042	139 \pm 36	.201 \pm .017	.139 \pm .036 \pm .018	3.50-3.90	3.70	.0020 \pm .0005 \pm .0003
.045-.052	.048	339 \pm 49	.262 \pm .019	.150 \pm .032 \pm .018	3.22-3.50	3.35	.0037 \pm .0008 \pm .0005
.052-.060	.056	145 \pm 46	.134 \pm .013	.163 \pm .052 \pm .022	3.00-3.22	3.11	.0058 \pm .0018 \pm .0008
.100-.300	.186	159 \pm 33	.029 \pm .004	.033 \pm .007 \pm .006	1.21-2.36	1.79	.0060 \pm .0012 \pm .0010
.300-.500	.384	66 \pm 21	.049 \pm .009	.008 \pm .003 \pm .002	0.70-1.21	0.96	.0032 \pm .0010 \pm .0007

Table 7: Differential cross-sections for $\Lambda(1520)$ as a function of x_E and $\xi \equiv \ln(1/x_p)$. Given are the statistical and those systematic error which affect the point-to-point cross-section. In the range $0.06 < x_E < 0.10$ no signal can be extracted due to ambiguities in the dE/dx particle identification.

particle	ALEPH	DELPHI	L3	OPAL	$\sqrt{s} \approx 10 \text{ GeV}$
proton	—	1.07 ± 0.14	—	0.92 ± 0.11	0.253 ± 0.016
Λ	0.386 ± 0.016	0.357 ± 0.017	0.37 ± 0.04	0.374 ± 0.010	0.080 ± 0.007
Σ^+	—	—	—	0.099 ± 0.015	—
Σ^0	—	0.070 ± 0.014	—	0.071 ± 0.018	0.023 ± 0.008
Σ^-	—	—	—	0.083 ± 0.011	—
$\frac{1}{2}[\Sigma^+ + \Sigma^-]$	—	0.085 ± 0.031	—	0.087 ± 0.009	—
$\frac{1}{3}[\Sigma^+ + \Sigma^0 + \Sigma^-]$	—	—	—	0.084 ± 0.009	—
Ξ^-	—	0.0250 ± 0.0023	—	0.0259 ± 0.0011	0.0059 ± 0.0007
Λ^{++}	—	0.079 ± 0.015	—	0.22 ± 0.06	0.040 ± 0.010
$\Sigma(1385)^\pm$	—	0.0382 ± 0.0053	—	0.0479 ± 0.0029	0.0106 ± 0.0020
$\Xi(1530)^0$	—	0.0041 ± 0.0006	—	0.0068 ± 0.0007	0.0015 ± 0.0006
Ω^-	—	0.0014 ± 0.0005	—	0.0018 ± 0.0004	0.0007 ± 0.0004
$\Lambda(1520)$	—	—	—	0.0213 ± 0.0028	0.008 ± 0.002

Table 8: Inclusive particle yields in from OPAL including data from [6,20,30] compared with published results from other LEP experiments [8,10–12,33–36] and with the average production rates for centre-of-mass energies near 10 GeV [19].

particle	OPAL	Jetset 7.3	Jetset 7.4	Herwig 5.6	Therm. Model
$n_{charged}$	21.05 ± 0.20	21.3	21.0	21.5	21.5
K^0	1.99 ± 0.04	2.03	2.21	2.35	2.02
proton	0.92 ± 0.11	1.16	1.20	0.83	1.07
Λ	0.374 ± 0.010	0.375	0.385	0.351	0.323
Σ^+	0.099 ± 0.015	0.070	0.072	0.072	0.077
Σ^0	0.071 ± 0.018	0.071	0.073	0.056	0.077
Σ^-	0.083 ± 0.011	0.066	0.067	0.060	0.069
Ξ^-	0.0259 ± 0.0011	0.0268	0.0274	0.0381	0.0243
Δ^{++}	0.22 ± 0.06	0.18	0.19	0.17	0.19
$\Sigma(1385)^+$	0.0239 ± 0.0015	0.0370	0.0381	0.0625	0.0347
$\Sigma(1385)^-$	0.0240 ± 0.0017	0.0346	0.0359	0.0574	0.0380
$\Xi(1530)^0$	0.0068 ± 0.0007	0.0052	0.0054	0.0146	0.0084
Ω^-	0.0018 ± 0.0004	0.0007	0.0007	0.0039	0.0017
$\Lambda(1520)$	0.0213 ± 0.0028	—	—	—	0.0172

Table 9: Inclusive particle yields per event in the data compared with Monte Carlo models and a thermodynamic model [44]. For the data the statistical and systematic errors are added in quadrature. The OPAL measured values for the charged multiplicity $n_{charged}$, K^0 , protons, Σ baryons, and Δ^{++} are taken from [41], [13], [6], [20], and [30], respectively. The values from JETSET are those obtained with its default tuning. Note that the $\Lambda(1520)$ is not present in either JETSET or HERWIG.

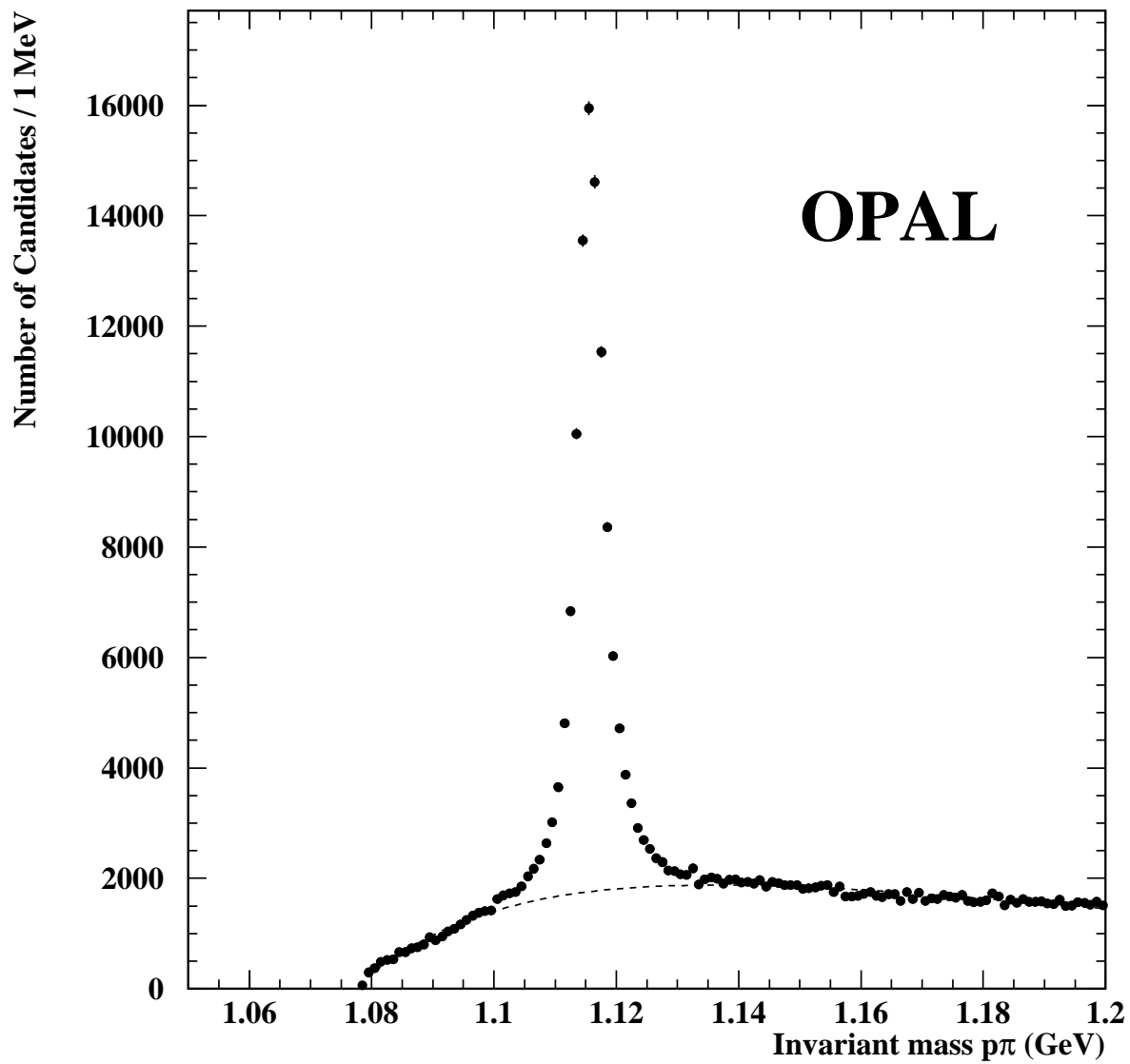


Figure 1: Invariant mass $p\pi$, method 1. The dashed curve is the result of the fit for the background.

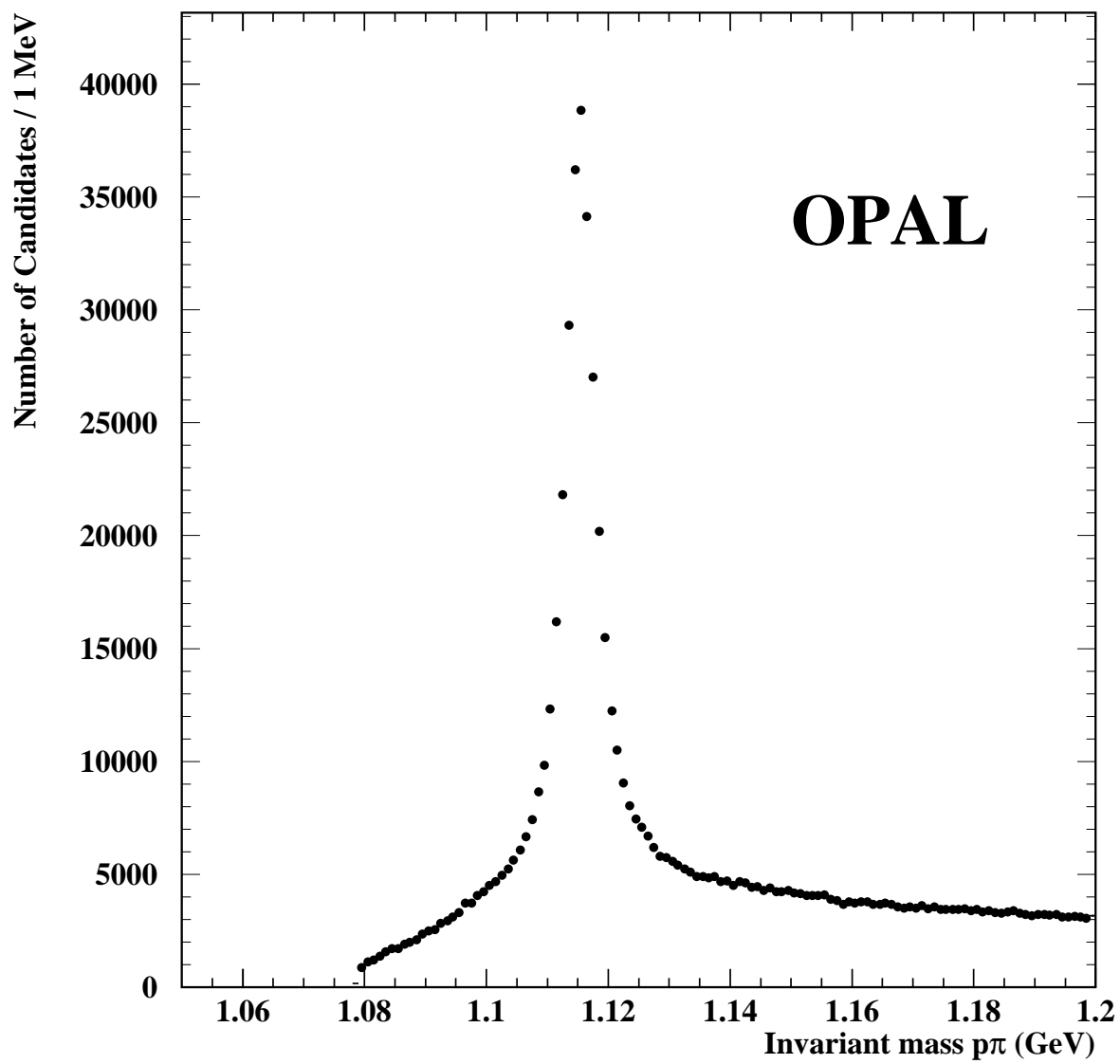


Figure 2: Invariant mass $p\pi$, method 2.

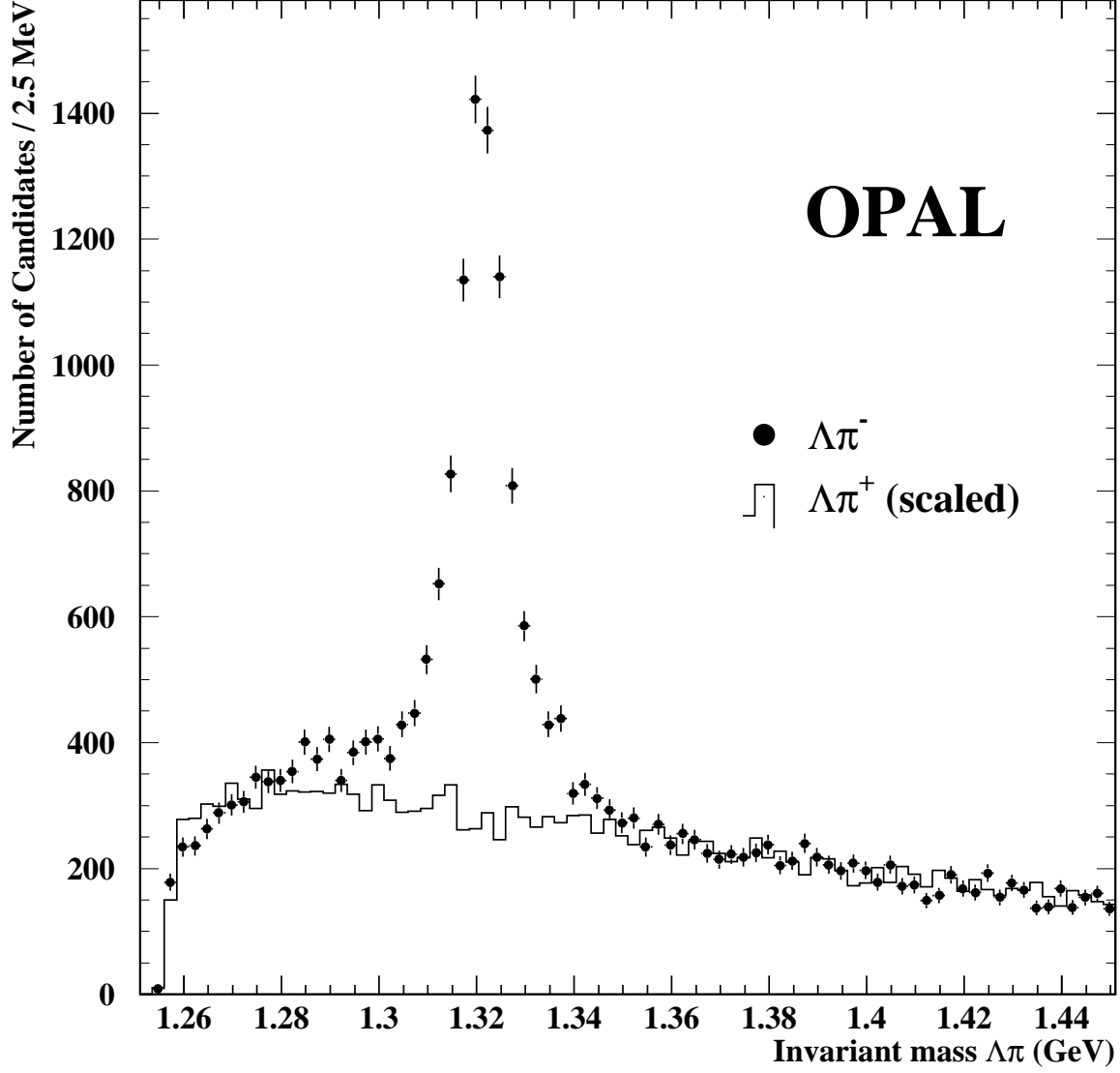


Figure 3: Invariant mass $\Lambda\pi^-$ (points with error bars), in which a Ξ^- peak can be clearly seen. The background is determined using the wrong charge combination $\Lambda\pi^+$, which has been scaled downwards to agree with the $\Lambda\pi^-$ distribution outside the signal region.

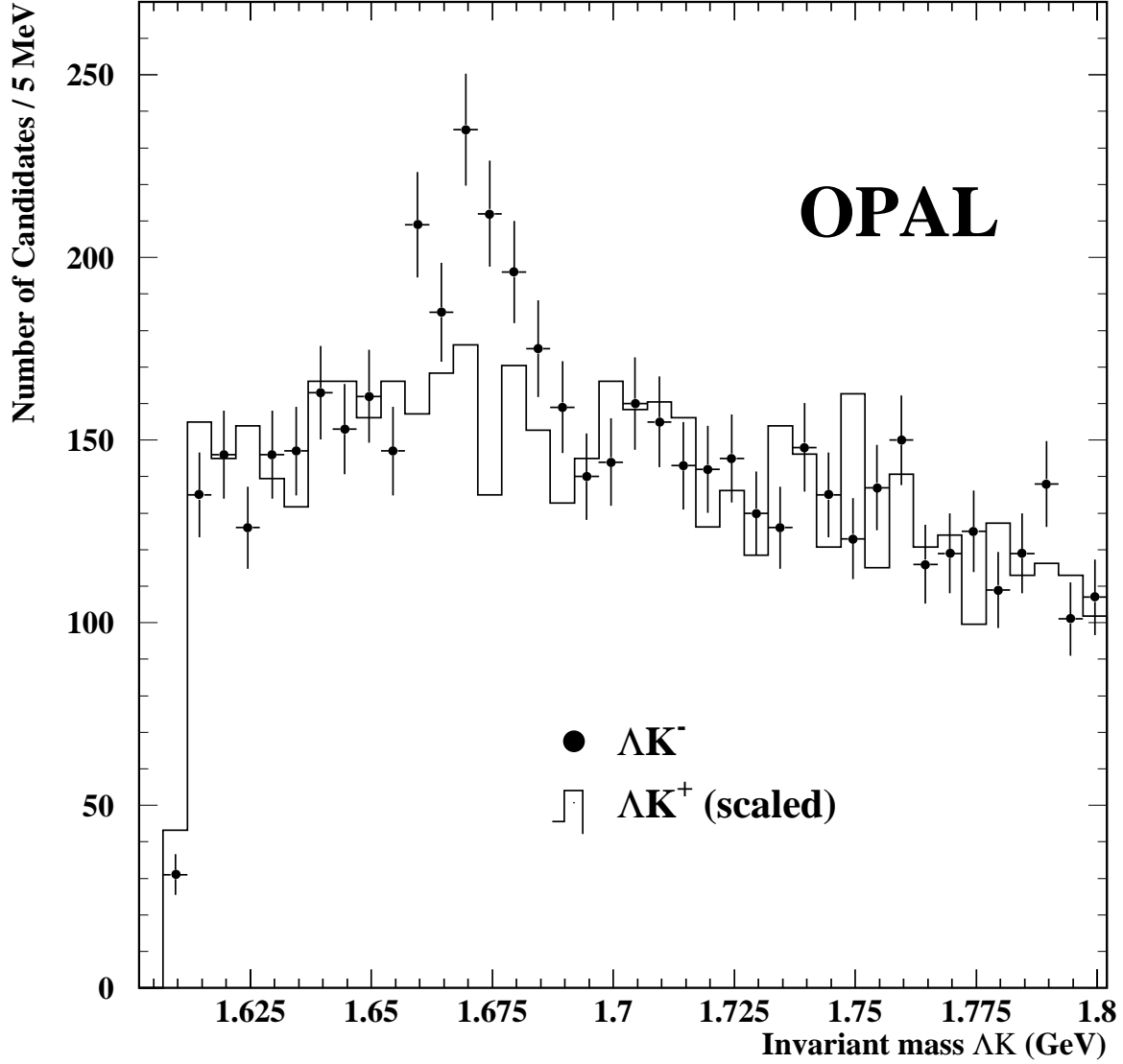


Figure 4: Invariant mass ΛK^- (points with error bars), in which an Ω^- peak is seen. Also shown is the wrong charge combination, ΛK^+ , which has been scaled upwards to agree with the ΛK^- distribution outside the signal region in order to determine the background.

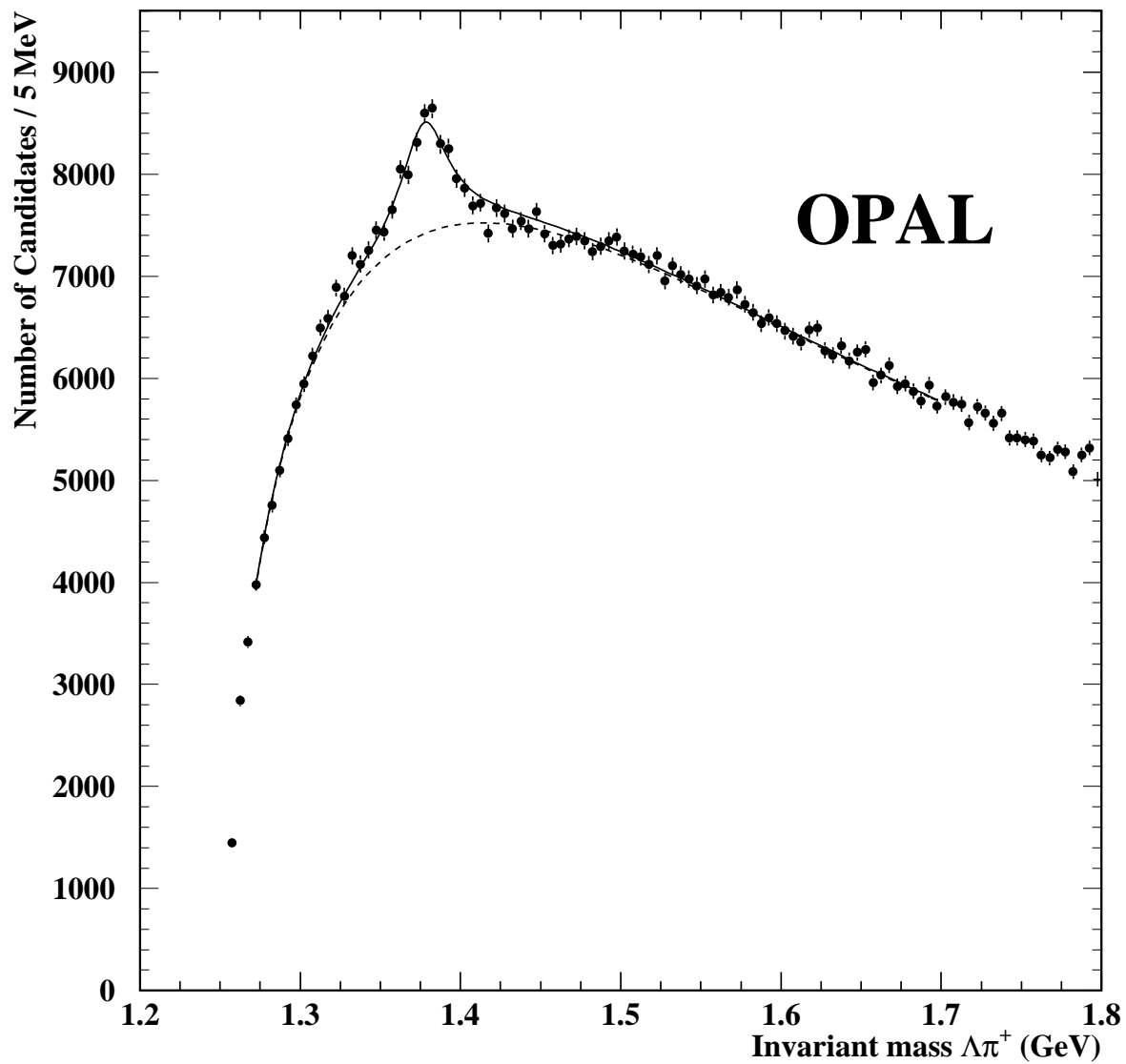


Figure 5: Invariant mass $\Lambda\pi^+$. A clear $\Sigma(1385)^+$ peak can be seen. The dashed curve is the result of the fit for the background and the solid curve the signal plus background.

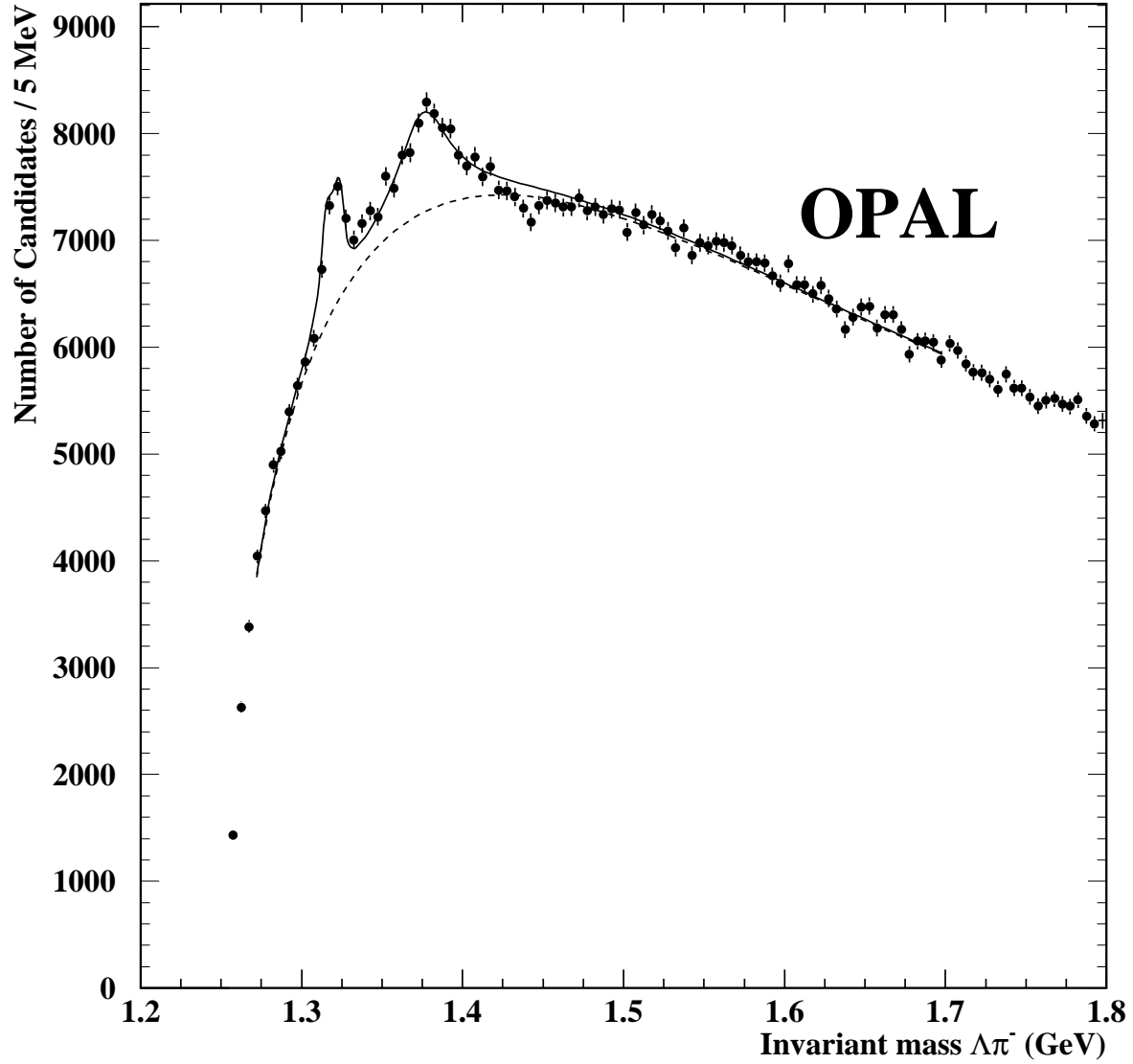


Figure 6: Invariant mass $\Lambda\pi^-$. A clear $\Sigma(1385)^-$ peak can be seen, as well as a residual Ξ^- peak. The dashed curve is the result of the fit for the background and the solid curve the fit to signal plus background.

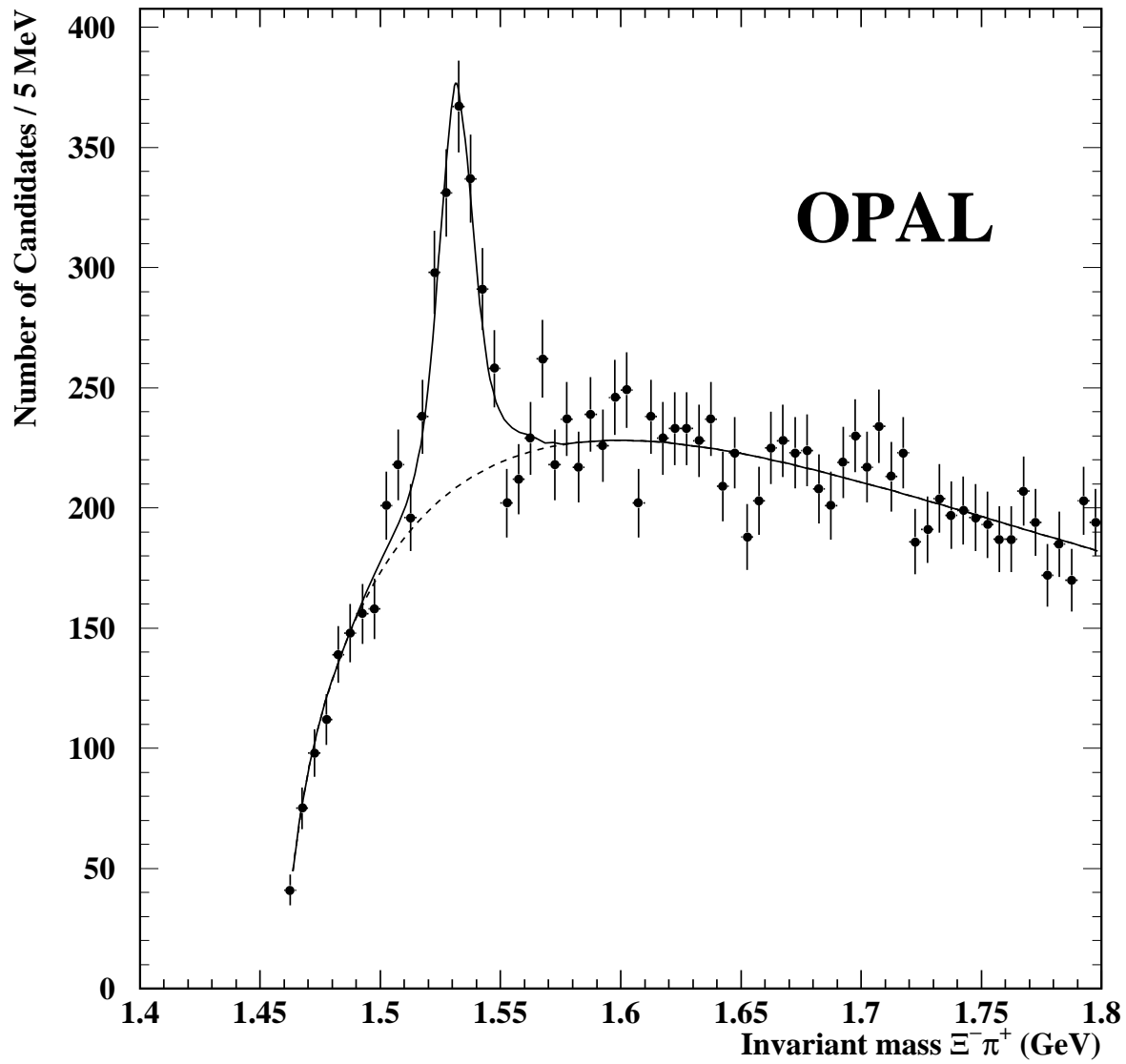


Figure 7: Invariant mass $\Xi^- \pi^+$. A $\Xi(1530)^0$ peak is observed. The dashed curve is the result of the fit for the background and the solid curve the fit to signal plus background.

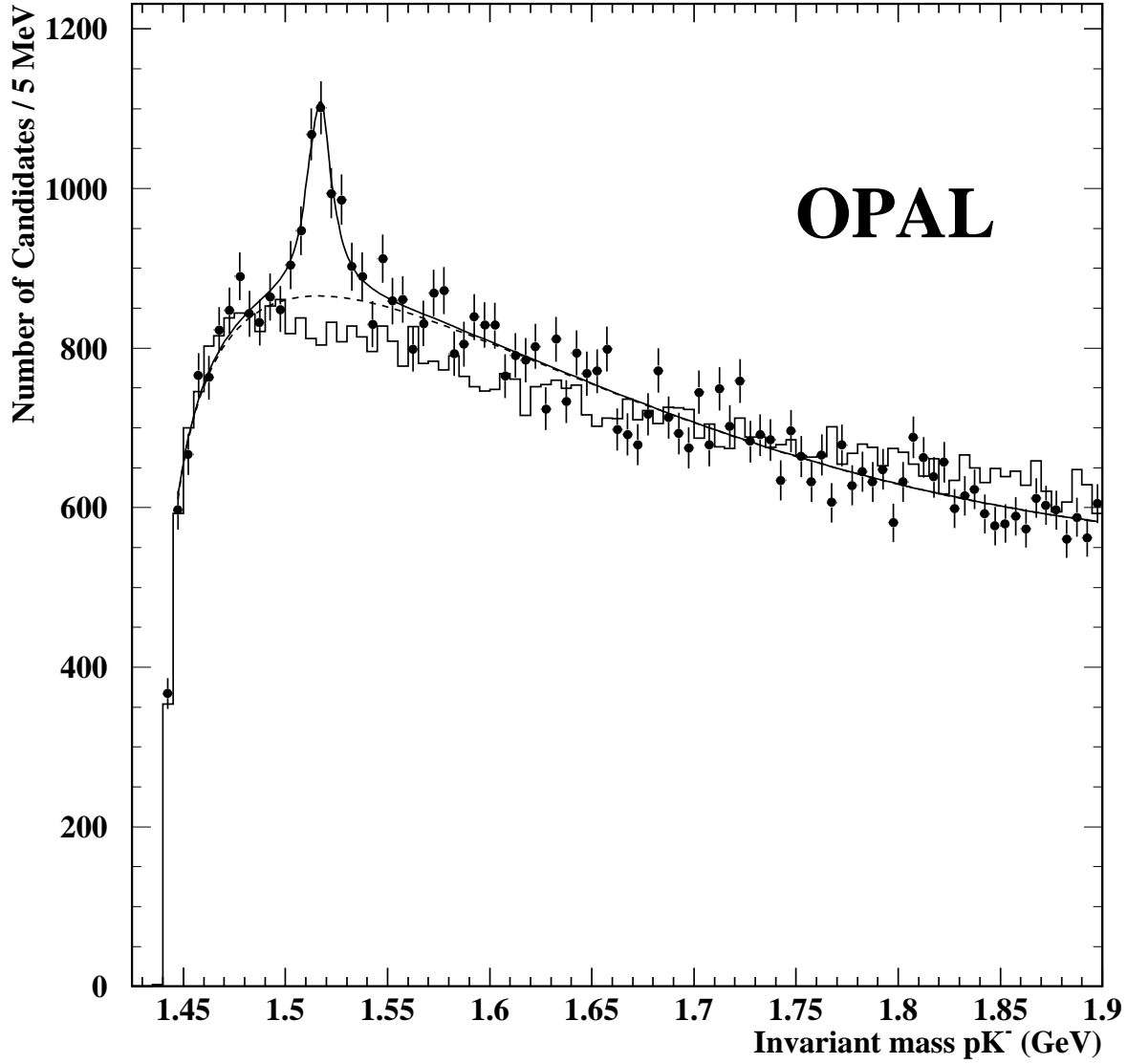


Figure 8: Invariant mass pK^- (points with error bars). A clear $\Lambda(1520)$ peak can be seen, while no peak is evident in the Monte Carlo (histogram). The dashed curve is the result of the fit for the background and the solid curve the fit to signal plus background.

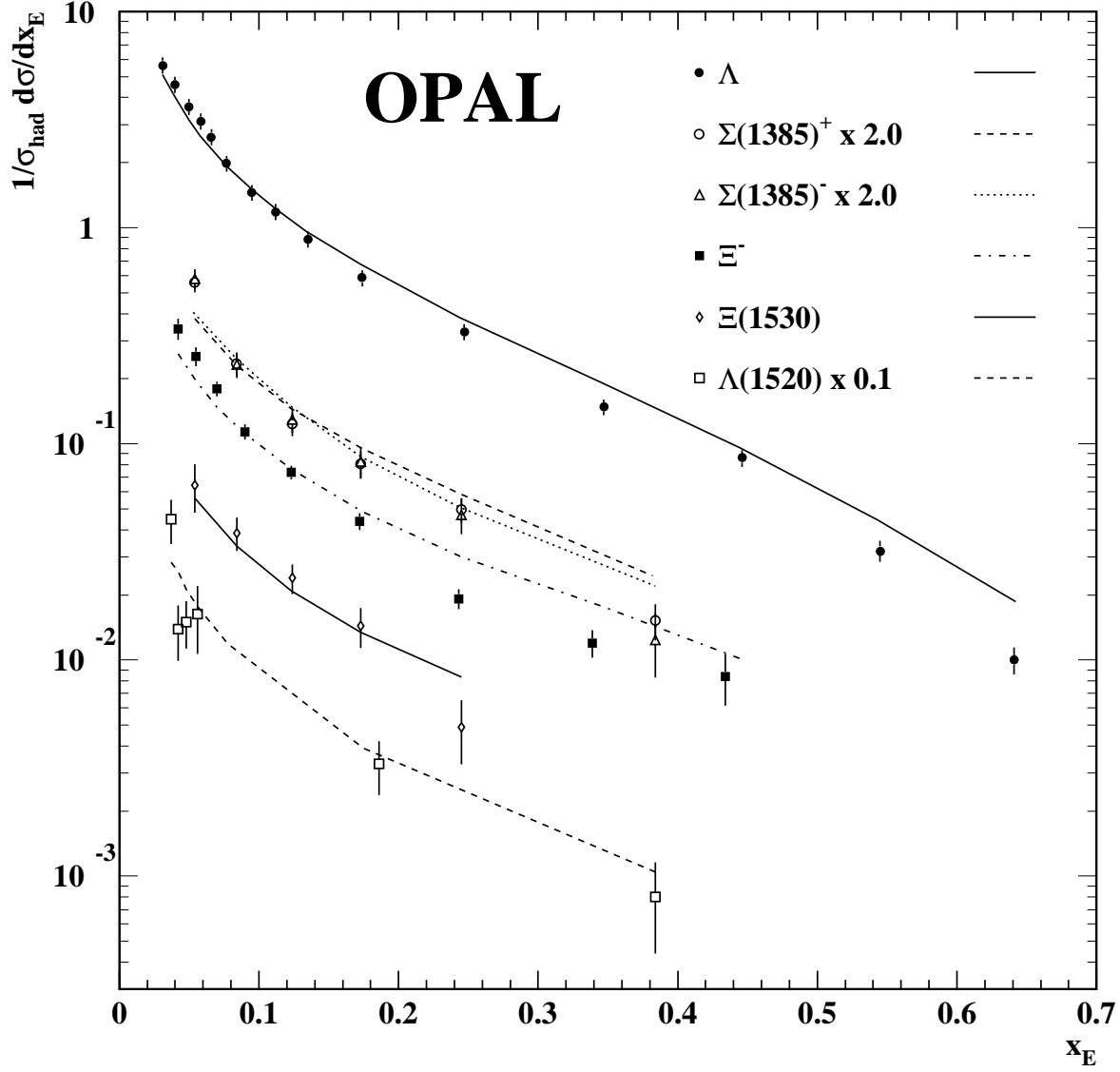


Figure 9: Differential cross-sections $(1/\sigma_{had})d\sigma/dx_E$ for Λ , $\Sigma(1385)^\pm$, Ξ^- , $\Xi(1530)$, and $\Lambda(1520)$. The $\Sigma(1385)^\pm$ and $\Lambda(1520)$ have been scaled by factors of 2 and 0.1, respectively, for clarity. The curves show the differential cross-sections predicted by JETSET 7.4, which has been binned in the same manner as the data and normalised to the event yield in the data. Since the $\Lambda(1520)$ is not present in JETSET, we compare the the $\Sigma(1385)^\pm$ differential cross-section shape from JETSET to the measured $\Lambda(1520)$ cross-section. The error bars show point-to-point statistical and systematic errors added in quadrature.

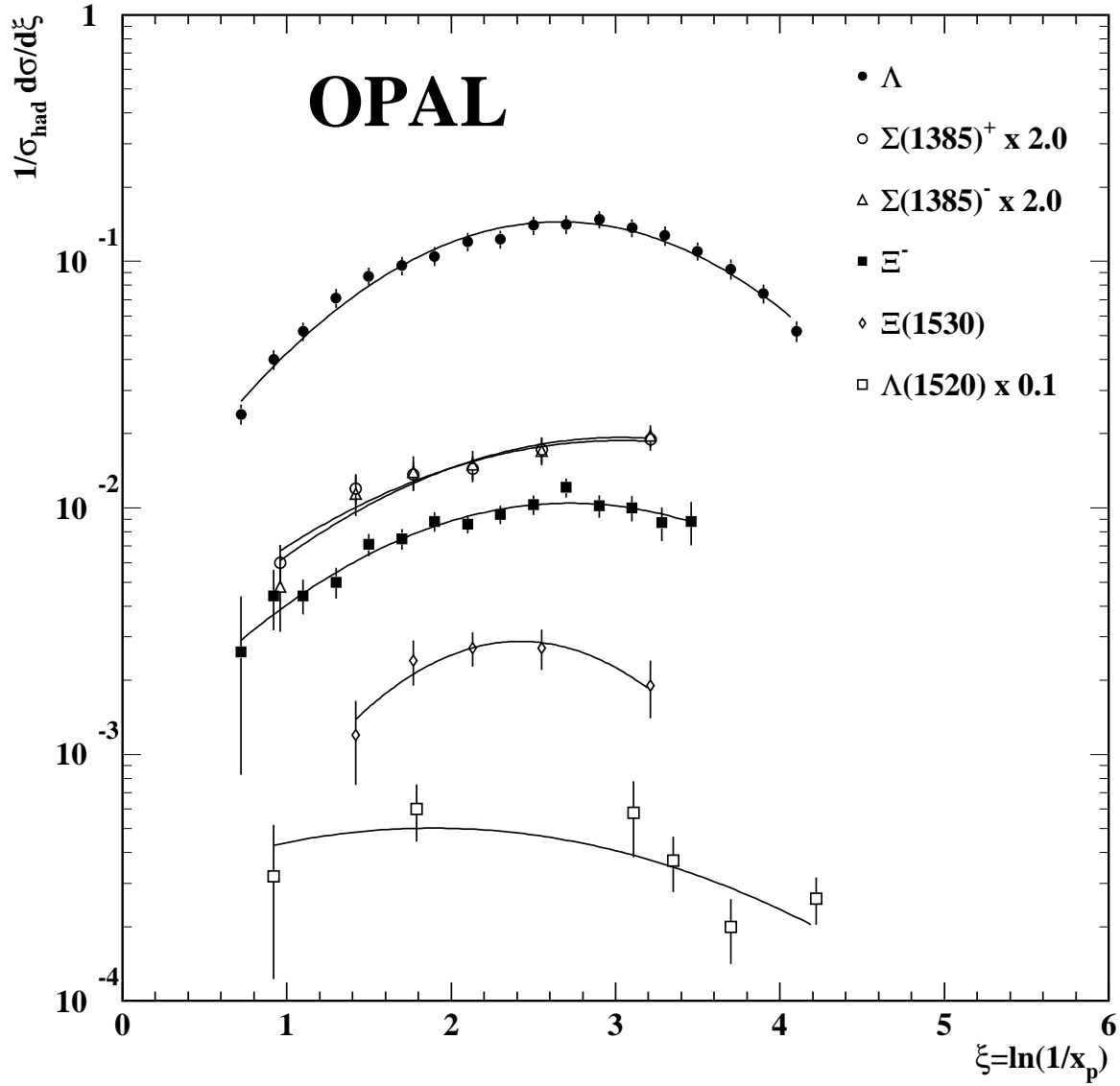


Figure 10: Differential cross-sections for Λ , $\Sigma(1385)^\pm$ (scaled upwards by a factor of 2), Ξ^- , $\Xi(1530)$, and $\Lambda(1520)$ (scaled downwards by an order of magnitude) as a function of $\xi \equiv \ln(1/x_p)$. The curves show Gaussian fits to the distributions made in order to determine the maximum ξ value. The error bars represent the point-to-point statistical and systematic errors added in quadrature.